Separation and Purification Technology 322 (2023) 124275

Contents lists available at ScienceDirect

Separation and Purification Technology

journal homepage: www.elsevier.com/locate/seppur

Tethering cellulose fibers with disulphide linkages for rapid and efficient adsorption of mercury ions and dye from wastewater: Adsorption mechanism and process optimization using RSM

Manpreet Kaur [a], Vijay Kumar [a], Kavita Sharma [a], Sumant Saini [b], Mukta Sharma [c], Christian Paulik [d], Hideaki Yoshitake [e], Gaurav Rattan [f], Anupama Kaushik [a,f,*]

[a] Energy Research Centre, Panjab University, Chandigarh, India
[b] School of Pharmaceutical Sciences, Lovely Professional University, Phagwara, Punjab, India
[c] Department of Civil Engineering, IKG Punjab Technical University, Jalandhar, India
[d] Institute for Chemical Technology of Organic Materials, Johannes Kepler University, Linz, Austria
[e] Division of Materials and Chemical Engineering, Yokohama National University, 79-5 Tokiwadai, Hodogaya-Ku, Yokohama 240-8501, Japan
[f] Dr. SSB UniversityInstitute of Chemical Engineering and Technology, Panjab University, Chandigarh, India

ARTICLE INFO

Keywords:
Raw hemp cellulose fibers
Dithiopropionic acid modified cellulose
Non-linear adsorption kinetics
RSM
Mercury (II) ions
Safranin O dye

ABSTRACT

Hemp stalks, readily available bio-waste in northern India, are good source of cellulose nanofibers (CNFs) with exceptional strength and stiffness. In this study, a facile route was envisaged to affix disulphide linkages on hemp derived CNFs (CNF-S-S-CNF) using 3,3-dithiopropionic acid. CNF-S-S-CNF with two sulphur groups on the cellulose backbone scored high selectivity for mercury ions (distribution coefficient of 5×10^5 mL.g^{-1}) owing to soft–soft interactions, besides exhibiting affinity for safranin O (SO) due to strong electrostatic attractions. Thermal stability up to 700 °C advocated high temperature applications of CNF-S-S-CNF. Response surface methodology (RSM) with Box Behnken Design (BBD) was applied using Design Expert software 13 for tuning the process parameters. Statistical analysis of variance (ANOVA) established a maximum adsorption capacity, q_e of 100% for Hg(II) ions achieved at optimum conditions of pH 5.5, Hg(II) concentration of 100 mg L^{-1} with adsorbent dosage of 100 mg and contact time of 9.50 min, while for SO, 100% adsorption was achieved at pH 6.5, SO concentration of 1 mg L^{-1} with adsorbent dosage of 60 mg and contact time of 9.50 min, in accord with the experimental results. Both, linear and non-linear kinetics and isotherm models were fitted to further understand the adsorption mechanism. The non-linear pseudo-second order demonstrated better adsorption kinetics for Hg(II), while SO fitted better to the linear pseudo-second order model. Ultra-rapid adsorption kinetics was achieved with pseudo second order rate constant, K_2 of 0.197 g.mg^{-1}.min^{-1} and 100% removal within 5 s (Co = 10 mg L^{-1}) of Hg(II) ions. FTIR and XPS confirmed strong interactions of CNF-S-S-CNF with Hg(II) ions accomplishing a maximum adsorption capacity, $q_{e\ exp}$ of 828.5 mg/g. Regeneration of adsorbent for 8 cycles with retention of 96% and 80% efficacy for Hg(II) ions and SO, respectively endorse its outstanding potential in wastewater remediation.

1. Introduction

Increasing industrialization and urbanization has led to surge in an inappropriate discharge of contaminants into the aquatic system. Among various pollutants, heavy metal ions, especially mercury, a naturally occurring element is one of the most noxious pollutants that accumulate in the water cycle and severely affect the living beings. According to the World Health Organization (WHO) the permissible limit of Hg(II) in drinking water is 0.002 mg L^{-1} [1]. Mercury is released into the environment from natural sources like volcanic eruptions, geothermal activities and through industrial processes *viz.* metal mining, non-ferrous metal smelting, textile production, dental amalgam fillings, artisanal gold production, waste incineration, coal combustion, refining and manufacturing industries leading to increased water pollution [2–5]. Mercury exists in three forms*: metallic mercury, inorganic mercury, and organic mercury*. Metallic mercury Hg(0), generally found in vapour

* Corresponding author at: Energy Research Centre, Panjab University, Chandigarh, India.
E-mail address: anupamachem@gmail.com (A. Kaushik).

https://doi.org/10.1016/j.seppur.2023.124275
Received 29 March 2023; Received in revised form 23 May 2023; Accepted 3 June 2023
Available online 7 June 2023

form has a high residence time ranging from 0.5 to 2 years and can be easily transported up to 1000 km and is deposited as inorganic mercury compounds or salts by combining with other elements such as oxygen, sulphur etc. in soil and water [6]. The other two forms are further converted into organic mercury through microbial reactions, which enter the food chain via marine eatables [7]. It accumulates in the body causing neurological disorders, damaging the brain tissues and even leads to kidney failure [5]. Consequently, there is an urgent need for rapid, specific and efficient methods for removal, of mercury [8].

Dental amalgam fillings artisanal small-scale gold production, waste incineration,

Besides, the growing population and urbanization has caused a massive upsurge in demand for textiles. About 10,000 dyes weighing around 7×10^5 tonnes are generated from various industrial processes. During the dyeing process, only 10–25% of dyes are consumed, while 2–20% are discharged directly in the water bodies as aqueous effluents. When these effluents get hydrolysed, toxic carcinogenic aromatic amines are generated, causing a severe threat to flora and fauna [9]. Safranin O (SO) (3,7-dimethyl-10-phenylphenazin-10-ium-2,8-diamine chloride) a water-soluble organic dye, generally known as basic red 2 dye is quite prevalent in textile industries. Exposure to SO causes eye burns, which can result in irreversible damage to the cornea besides causing respiratory tract discomfort, making it imperative to remove it from the effluents before their discharge.

Amongst many techniques available for removal of pollutants, including chemical precipitation [10], membranes separation [11], ion exchange [12] and adsorption [13,14], adsorption is the preferred technique owing to its low cost, efficient removal capacity, facile usage and good reversibility [15]. Extensive reports are available on adsorbents based on clay minerals, metal oxides, zeolites, activated carbon, metal organic frameworks etc. for the removal of metal ions. However, they lack specificity, have limited adsorption ability and cause secondary pollution. Biomass derived cellulose nanofibers offer many advantages like cost-effectiveness, abundance in nature, biodegradability and environmental sustainability. Furthermore, the plenty of surface hydroxyl groups available for modification, excellent specific strength, extraordinary surface area, and outstanding thermal and chemical stability make CNFs good contender as adsorbents. Hemp, *Cannabis sativa*, is a wild plant widely grown in Northern India. The leaves and seeds of the plant are rich in phytochemicals and bioactive components and thus are used in medical applications, while hemp stalks are often discarded [16]. These stalks containing bast fibres are a good source of cellulose (≈76%) with exceptional strength and stiffness. It was thus thought prudent to use hemp as a source of cellulose for this study.

A common approach in designing an efficient adsorbent is to introduce functional groups on the surface of adsorbent for selective interaction with the analyte molecule, without compromising with the surface area and porosity. A large number of functional groups including thiols, carbonyls, amines, sulphides etc. have been introduced to enhance the adsorption capacity of cellulose for the removal of Hg(II) ions and textile dyes [17,18]. Velempini et al. used cysteamine for the synthesis of carboxymethyl cellulose thiol-imprinted polymer for selective adsorption of Hg(II) ions having an adsorption capacity of 80 mg/g [19]. Thiolated spherical cellulose has been reported for the removal of Hg(II) ions with a maximum adsorption capacity of 404.95 mg/g and 98.6% removal from 100 ppm solution [20]. However, when reused, the removal efficiency reduced significantly. Moreover, most of the reported thiol modified cellulose based adsorbents exhibit slow adsorption kinetics, low adsorbing capacity and modest selectivity.

Apart from modified cellulose, some studies have also been reported for annihilation of Hg(II) ions using biomass based nanocomposites. Recently, Liu et al synthesized rice straw based biochar with high surface area of 2372.52 $m^2\ g^{-1}$ with rich pore structure [21]. The biochar yielded a moderate adsorption capacity of 209.65 mg g^{-1}. Magnetic bio composites with curcumin and iron oxide nanoparticles have been reported as outstanding adsorbent for Hg(II) ions with maximum adsorption capacity of 144.9 mg g^{-1} by Naushad et al. [22]. Tannic acid cross-linked cellulose/ polyethyleneimine functionalized magnetic composites were reported to yield 99% removal of Hg(II) ions with adsorption capacity of 247.51 mg g^{-1} by Sun et al. [23]. CNF decorated with aminophosphonic acid functionalised ZrO_2 nanoparticles were reported to exhibit Lewis soft–soft interactions with Hg(II) ions yielding an adsorption capacity of 180 mg g^{-1} [24]. The cellulose based composites although exhibited good recyclability, however, the synthesis procedure was very complicated and the maximum adsorption capacity was limited.

Although lots of work has been reported on different modifications on cellulose, the disulphide (-S-S-) group having twice the number of sulphur atoms as compared to sulphide and having a high affinity for Hg (II) ions has never been anchored on cellulose backbone. In this study, CNFs extracted from hemp bast fibres were modified using 3,3-dithiopropionic acid to yield a porous CNF network with disulphide linkages affixed throughout (CNF-S-S-CNF.) It was hypothesized that the introduction of two sulphur groups in the cellulose network will engender strong soft–soft interactions with Hg(II) ions resulting in ultra-fast adsorption kinetics. The novelty of the current work is thus the insertion of disulphide linkages on the CNF backbone, not reported previously, which concurrently garnered distinct benefits of ultra-rapid, highly selective and effective capture of Hg(II) ions and SO dye. The process parameters were optimized using response surface methodology (RSM) and linear and non-linear kinetic and isotherm models were applied to understand the adsorption mechanism. CNF-S-S-CNF exhibited high thermal stability, facile recoverability and appreciable reusability owing to strong fibrous structure of cellulose, which aids in rapid diffusion of analyte molecules.

2. Materials and methods

2.1. Reagents

Sodium hydroxide (NaOH), hydrogen peroxide (H_2O_2) (30% v/v), hydrochloric acid (HCl) (30%), urea, N,N-carbonyldiimidazole (AR, 98%) and sodium acetate were bought from Sisco Research Laboratories (SRL), India. 3,3-Dithiopropionic acid (DTPA), dimethyl sulphoxide (DMSO), SO dye, mercuric acetate (MA), Micheler's thioketone [4,4-bis (dimethylamino) thiobenzophenone] (TMK) were obtained from Tokyo Chemical Industry (TCI).

2.2. Extraction of pristine cellulose fibers (PCFs) from hemp bast fibers (HBFs)

Hemp stalks (RH) were gathered from the neighbouring fields of Punjab, India. The stalks were dipped overnight in water to soften the outer bast fibers layer. Thereafter, the bast fibers were manually separated from hemp stalks, and dried. Extraction of cellulose was achieved using previously reported protocol [25]. The schematic has been elucidated in Fig. 1(a) and the details of the process has been given in section S1, supplementary data file.

2.3. Synthesis of dithiopropionic grafted cellulose fibers (CNF-S-S-CNF)

To regenerate cellulose fibres, 2 gm PCFs were dissolved in a precooled solution of 7% NaOH/ 12% urea/ 81% H_2O and left overnight at −20∘C. After approximately 18–20 h when the solution get thawed, the mixture was ultracentrifuged to remove undissolved impurities [26]. Separately, CDI (3.0 gm, 18.5 mmol) was dissolved in 30 mL DMSO in another conical flask followed by the addition of 3 gm DTPA. CDI acts as activating agent for carboxylic groups on the surface of DTPA. The mixture was agitated overnight and then added to above PCFs solution. The reaction mixture was heated at 80∘C with continued stirring under N_2 atmosphere for 24 h. The resultant homogeneous mixture was precipitated by adding 500 mL ethanol to obtain disulphide grafted

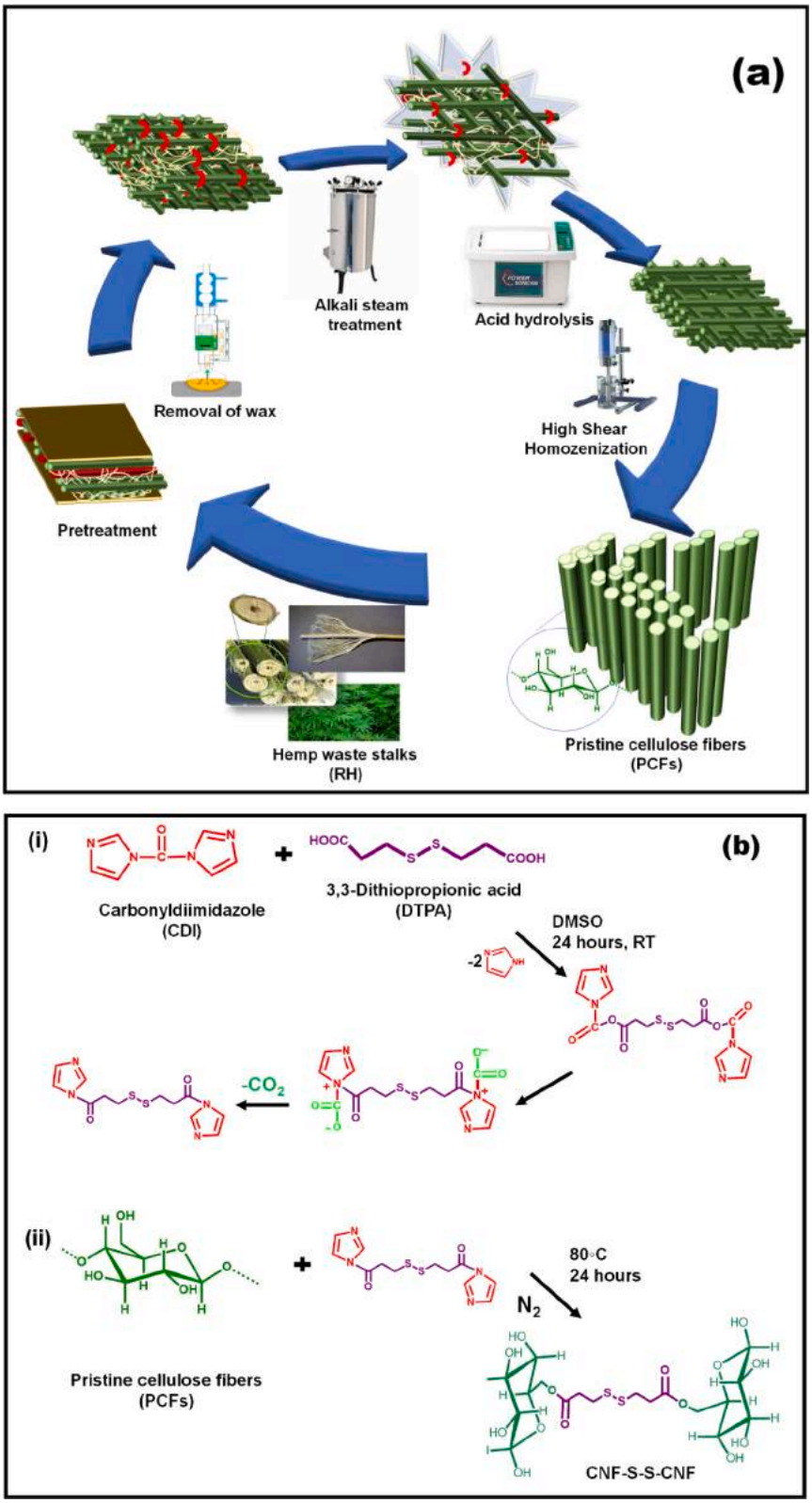

Fig. 1. (a). Steps for the extraction of Pristine cellulose fibers (PCFs) from raw hemp bast fibers (RH) (b) Grafting of Dithiopropionic on cellulose fibers (CNF-S-S-CNF).

cellulose fibers (CNF-S-S-CNF). The precipitates were then filtered and washed with water followed by washing with ethanol. The final product was dried at 50 °C under vacuum conditions [27]. The reactions involved in the disulphide modification of cellulose fibers have been illustrated in Fig. 1(b).

Peracylation of the leftover hydroxyl groups was carried out in order to estimate the degree of substitution and structure of CNF-S-S-CNF using 1H NMR spectroscopy. 0.2 g of CNF-S-S-CNF was taken along with 7 mL each of pyridine and propionic anhydride in a 100 mL round bottom flask. 0.2 g of 4-dimethylpyridine was then added as a catalyst, following 24 h of stirring at 80 °C. The mixture was finally cooled to room temperature and precipitated in 300 mL of ethanol. The precipitates were then filtered and washed with ethanol and dried in a vacuum oven at 60 °C [28].

2.4. Characterizations of PCFs and CNF-S-S-CNF

The chemical composition analysis and morphological characterizations of the RH, PCFs and CNF-S-S-CNF were accomplished using several techniques such as FTIR, XRD, FESEM-EDX, TGA, ^{1}H NMR and XPS (details given in section S2, supplementary data). American Society for Testing and Materials (ASTM1103-55 T) standard was used to evaluate the α-cellulose content using equation (1).

$$\alpha - Cellulose(\%) = \frac{weightofdrycellulose - celluloseresidue}{initialweightofdryHS \times moisturefreecontent} \times 100 \quad (1)$$

The grafting yield estimates the weight percent of grafted monomer on the cellulose backbone [29]. The yield of dithiopropionic grafted cellulose (CNF-S-S-CNF) was calculated using equation (2)

$$Graftingyield(\%) = \frac{WeightofdryCNF - S - S - CNF - WeightofinitialPCFs}{WeightofinitialPCFs} \times 100 \quad (2)$$

2.5. Batch adsorption experiments

2.5.1. Determination of zero-point charge (ZPC)

Optimal pH for the adsorption of Hg(II) metal ions and SO dye on the surface of CNF-S-S-CNF was calculated *via* surface charge determination. The ZPC of CNF-S-S-CNF was evaluated using a standard procedure given in section S3, supplementary file.

2.5.2. Removal of Hg(II) ions and Safranin-O dye

All adsorption studies for Hg(II) and SO were carried out at room temperature. The standard solution of Hg(II) ions (100 mg L^{-1}) was prepared by dissolving 15.9 mg of MA in 100 mL distilled water. Similarly, the standard solution of 100 mg L^{-1} for SO dye was prepared by dissolving 10 mg of SO dye in 100 mL of distilled water. Stock solutions were prepared by further diluting the standard solutions. The Hg(II) solution aliquots were analysed on UV-spectrophotometer using TMK which forms a blue-green coloured complex in ratio 1:1 with Hg(II) and gives an absorption maxima at λ = 590 nm [30]. This peak at 590 nm was measured to determine the concentration of Hg(II) ions while the peak at 520 nm was considered for SO dye at various stages of adsorption. [25]. For adsorption tests, 100 mL of adsorbate solution of different concentrations ranging (10–1000 mg L^{-1} for Hg(II) ions and 5–30 mg L^{-1} for SO dye) were placed and 100 mg of CNF-S-S-CNF were added to each sample run. The solution was continuously stirred and at various time periods, 4 mL aliquots were collected and centrifuged to separate the adsorbent. The concentration of Hg(II) ions in the aliquots was determined using an Agilent Cary UV–Vis spectrophotometer.

2.5.3. Selectivity of metal ions and effect of pH

Initially, the selectivity of CNF-S-S-CNF towards the adsorption of Hg (II) in presence of other interfering metal ions was assessed. Adsorption tests were carried out by taking 10 mg of CNF-S-S-CNF in 10 mL of 10 mg L^{-1} of Hg(II) ions with different metal ions: Cu(II), Cd(II), Pb(II), Fe(III), Cr(III), K(I), Na(I), Ca(II) and Zn(II) with the same concentration as mercury. Hg(II) ions gave the maximum adsorption, hence, all parametric studies were carried out with them. Amongst various parameters affecting adsorption including pH, contact time, adsorbent and adsorbate dosage, the pH has a most significant influence on the surface properties of adsorbent. Hence, the effect of pH was studied in the pH range of 1–7 using dilute 0.1 M HCl and 0.1 M NaOH in an aqueous medium. The percentage removal of pollutant and adsorption capacity (mg g^{-1}) at any time t (q_t) were determined using equations (3) and (4)

$$Removal(\%) = \frac{C_o - C_t}{C_o} \times 100 \quad (3)$$

$$Adsorptioncapacity(q_t) = \frac{(C_o - C_t)}{m} \times v \quad (4)$$

Where, C_o and C_t (mg L^{-1}) are the initial and residual concentrations at any time 't' of Hg(II), respectively, V(L) is the volume of adsorbate solution and w(g) is the weight of CNF-S-S-CNF.

2.6. Experimental design using response surface methodology (RSM)

One of the approaches for experimental design that is frequently used for process analysis and modelling is Response Surface Methodology (RSM). With RSM, the interaction of potential influencing factors on desired responses can be examined with the least amount of specified trials, making it simpler to get the ideal process conditions. Various parameters such as pH, initial adsorbent and adsorbate concentration and contact time were established as the most contributing parameters that were evaluated in five levels to analyse the adsorption efficiency of CNF-S-S-CNF as given in the Table S1, Section S5, supplementary data. RSM was used based on the Box Behnken Design (BBD) using Design Expert software 13. For the experimental design containing four parameters, 29 randomized controlled were suggested with 5 replicate runs around the central point. Analysis of variance (ANOVA) was used to evaluate the significance of variables and their interactions [31,32].

2.7. Adsorption kinetics and isotherms

The adsorption kinetics analyses the adsorption rate of adsorbate on the surface of adsorbent, the adsorbent performance as well as the mass transport phenomenon in a water treatment process[33]. To understand the adsorption mechanism of Hg(II) and SO on CNF-S-S-CNF, various kinetic models were used. Four linear models, pseudo first order (PFO), pseudo second order (PSO), Elovich model and intra particle diffusion model, while two non-linear forms, pseudo first order (NL-PFO), pseudo second order (NL-PSO) were used for in-depth analysis of mechanism. The model equations for all the models are given in Table 1. To assess the interaction between CNF-S-S-CNF and pollutants, experimental results were fitted into two isotherm models, Langmuir and Freundlich models, using both linearized and non-linearized forms, as elucidated in Table 1.

2.8. Error functions

The accuracy of kinetic and isotherm models was studied through comparison of four error functions i.e. coefficient of determination (R^2), adjusted coefficient of determination (R^2_{adj}), chi square (χ^2), root mean square error (RMSE) and error sum of squares (RSS) illustrated in equations (15), (16), (17), (18) and (19), respectively

$$R^2 = \frac{\sum_{i=1}^{n}\left(q_{e,cal} - q_{e,exp}\right)_i^2}{\sum_{i=1}^{n}\left(q_{e,cal} - (\overline{q}_{e,exp})\right)_i^2} \quad (15)$$

Table 1
Linear and non-linear kinetics and isotherm models.

	Linear equation	Non-linear equation	Constant
Lagergren pseudo first order (PFO) [34]	$\ln(q_e - q_t) = \ln q_e - k_1 t$(5) Where, q_t (mg g^{-1}) and q_o (mg g^{-1}) denotes adsorption capacities at time 't' and at equilibrium, respectively	$q_t = q_e(1 - e^{-k_1 t})$(6)	k_1 (min^{-1}) is pseudo first order rate constant
Pseudo second order (PSO) [35]	$\frac{t}{q_t} = \frac{1}{k_2 q_e^2} + \frac{1}{q_e} t$(7)	$q_t = \frac{k_2 q_e^2 t}{1 + k_2 q_e t}$(8)	k_2 (g $mg^{-1}.min^{-1}$) is second order rate constant
Elovich model	$q_t = \frac{1}{\beta}\ln(\alpha\beta) + \frac{1}{\beta} \ln t$(9)		α (m.mol g^{-1} min^{-1}) and β (g.$mmol^{-1}$) are experimental constants
Weber and Morris intra-particle diffusion	$q_t = k_{int} t^{1/2} + C$(10)		k_{int} (mg g^{-1}. $min^{1/2}$) is represents intra-particle diffusion constant and C (mg g^{-1}) is related to boundary layer thickness
Langmuir isotherm [36]	$\frac{C_e}{q_e} = \frac{1}{q_m K_L} + \frac{C_e}{q_m}$(11)Where, C_e (mg L^{-1}) and q_e (mg g^{-1}) indicates the concentration of adsorbate and adsorption capacity of adsorbent at equilibrium, respectively and q_m (mg g^{-1}) is maximum adsorption capacity	$q_e = \frac{q_m . k_L . C_e}{1 + k_L . C_e}$(12)	K_L (L mg^{-1}) the Langmuir constant, represents the affinity between adsorbate and adsorbent
Freundlich isotherm [37]	$\ln q_e = \ln k_F + \frac{1}{n} \ln C_e$(13)	$q_e = k_F . C_e^{\frac{1}{n}}$(14)	K_F ((mg g^{-1}) (L mg^{-1})) is the Freundlich constant and n is adsorption intensity

$$R^2_{adj} = 1 - \left[\frac{(1 - R^2)(n - 1)}{n - k - 1}\right] \quad (16)$$

$$\chi 2 = \sum_{i=1}^{n} \frac{(q_{e,exp} - q_{e,cal})^2}{q_{e,cal}} \quad (17)$$

$$RMSE = \sqrt{\frac{1}{n}\sum_{i=1}^{n} (q_{e,exp} - q_{e,cal})^2} \quad (18)$$

$$SSE = \sum_{i=1}^{n} (q_{e,exp} - q_{e,cal})^2 \quad (19)$$

Where, n denotes the number of experimental points, $q_{e,\,exp}$ (mg g^{-1}) and $q_{e,\,cal}$ (mg g^{-1}) are the experimental and theoretical values of adsorption at equilibrium, while K signifies the number of independent variables.

2.9. Desorption and regeneration studies

To render the adsorption economically sustainable, the adsorbent should be retrievable and recyclable multiple times via the adsorption and desorption process. To recover the adsorbent, the saturated CNF-S-S-CNF was treated with a 100 mL mixture of 0.1 M thiourea and 0.1 M HCl for 5 h to remove the adsorbed Hg(II) ions. To remove SO dye, similar procedure was followed with the exception that CNF-S-S-CNF was recovered only using 0.1 M HCl. The regenerated CNF-S-S-CNF was separated by centrifuging and washing and further used for 8 cycles to assess their adsorption efficacy.

3. Results and discussion

3.1. Extraction and functionalization of PCFs

The cellulose, hemicellulose and lignin content of raw hemp (RH) fibres and pristine cellulose fibers after the chemico-mechanical process were determined. The RH initially had 57.20 % cellulose, 9.6% hemicellulose and 5.3% lignin, while after the treatment, the cellulose content increased to 88.9%, whereas the lignin and hemicellulose content reduced to 7.02% and 3.1 %, respectively. The grafting yield of CNF-S-S-CNF and propionylated CNF-S-S-CNF was 90.2% and 78.4%, respectively. The degree of substitution (DS) of CNF-S-S-CNF was found to be 0.66, which was calculated by using ^{1}H NMR spectroscopy after per-propionylation explained in section S4, supplementary file.

3.2. Characterization of PCFs and CNF-S-S-CNF

To assess the changes in chemical bonding, and molecular structure that occurred during different stages of extraction and surface modification of the fibers, FTIR spectra of RH, PCFs and CNF-S-S-CNF were observed in the range of 500–4000 cm^{-1} (Fig. 2(a)). In all three spectra, the absorption bands at 3426 cm^{-1}, 2920 cm^{-1}, 1630 cm^{-1}, and 1440 cm^{-1} are attributed to hydroxyl group (O–H), aliphatic C–H stretching vibrations, absorbed water O–H bending vibrations and in-plane bending vibrations of HCH and OCH, respectively [38,39]. The vibration bands at 1734, 1510 and 1249 cm^{-1} in RH correspond to ether and ester bonds in hydroxycinnamic acids (p-coumaric and ferulic acids), present in lignin and hemicellulose and aromatic C = C stretching bands of lignin, respectively, which are absent in PCFs, confirming the removal of lignin during the extraction process [40,41]. The absorption peaks at 1163, 897 and 1031 cm^{-1} are attributed to the C-O-C asymmetric vibrations, β-glycosidic linkages and pyranose ring structure vibrations of PCFs, respectively [42]. In the FTIR spectra of CNF-S-S-CNF, the vibration bands appeared at 1730 and 1290 cm^{-1} for C = O and C-O stretching in the acetate group, confirming the successful grafting of DTPA on cellulose [43]. New absorption band at 627.27 cm^{-1} represents C-S bonding vibrations corresponding to C-SS-C bond of CNF-S-S-CNF [44].

The crystallinity of RH, PCFs, and CNF-S-S-CNF was evaluated using X-ray diffraction analysis presented in Fig. 2(b). The PCFs diffractogram reveals a prominent crystalline peak at 22.67° 2θ, corresponding to the 002 crystallographic diffraction plane of hydrogen bound sheets of cellulose I (I_α and I_β) configuration. The other three common peaks at 2θ = 15.42° (1 1 0), 16.4° (10–1) and 34.4° (0 4 0) suggest the retention of cellulose Iβ crystalline structure after the treatment [42]. The crystallinity index of PCFs was calculated using equation (20)

$$CrystallinityIndex(CI) = \frac{I_{002} - I_{am}}{I_{002}} \times 100 \quad (20)$$

Where, I_{002} and I_{am} refer to the crystalline phase and amorphous phase at 2θ = 22.7° and 18°, respectively. The crystallinity index increased from 58.2 % for RH to 78.7 % for PCFs with chemico mechanical treatment. In the XRD spectra of CNF-S-S-CNF, the diffraction peaks observed at 2θ = 11.48°, 20.24° and 21.86° correspond to (1 1 0), (10–1) and (0 0 2) diffraction planes, respectively, suggest the conversion of cellulose I to cellulose II during regeneration [45]. The XRD peaks at 26.39° and 28.00° appear due to the sulphide bonds present in CNF-S-S-CNF [46]. Other peaks at 30.42°, 35.37°, 38.13° and 41.57° are characteristic peaks of different forms of sulphur such as sulphide, thiol and free sulphur, further confirming the grafting of disulphide [47].

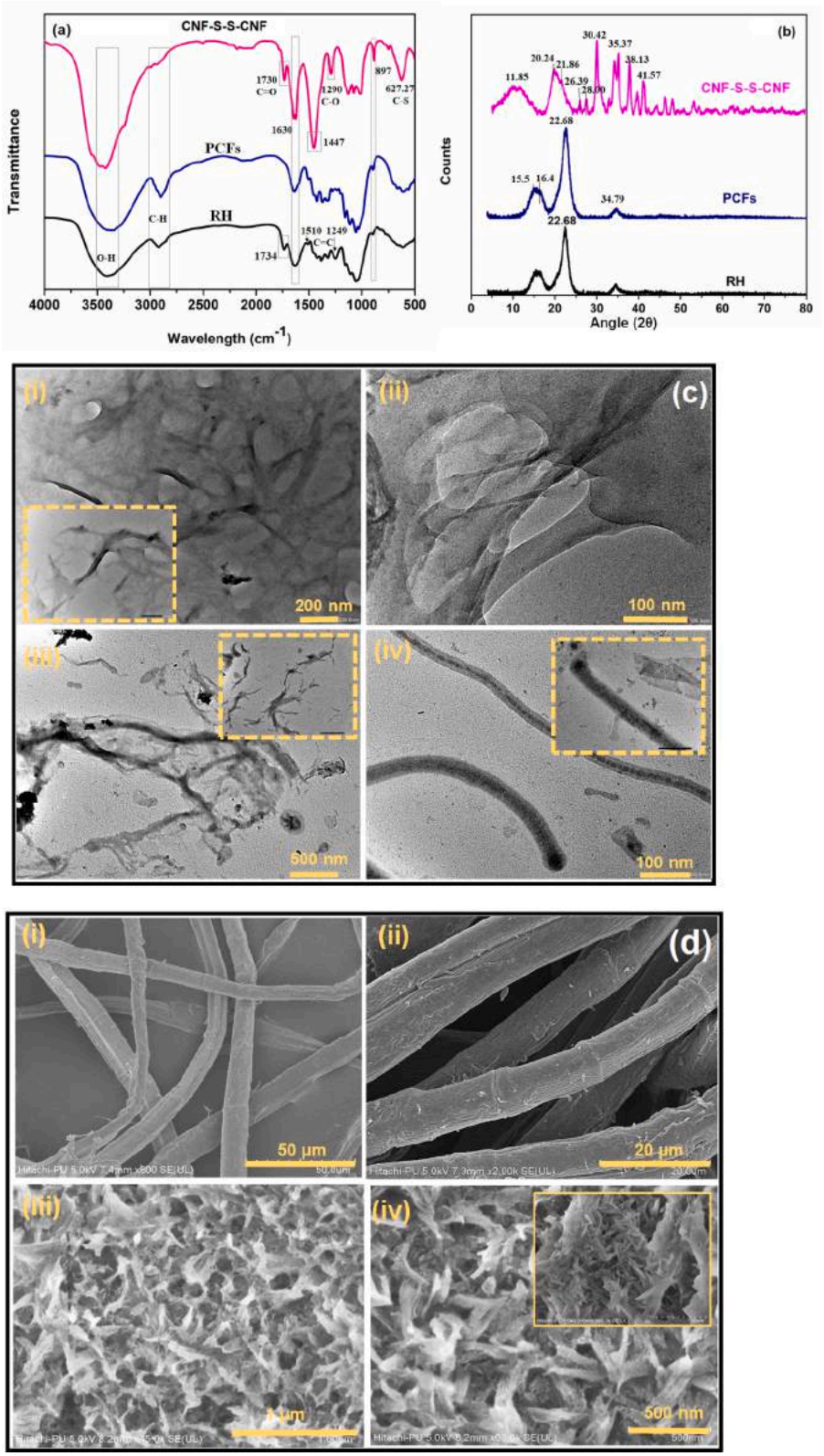

Fig. 2. (a) FTIR (b) XRD spectra of RH, PCFs and CNF-S-S-CNF (c) HR-TEM and (d) FESEM images of PCFs and CNF-S-S-CNF (e) EDX spectra of PCFs, CNF-S-S-CNF and CNF-S-S-CNF loaded with Hg(II) and SO (f) TGA analysis of RH, PCFs and CNF-S-S-CNF.

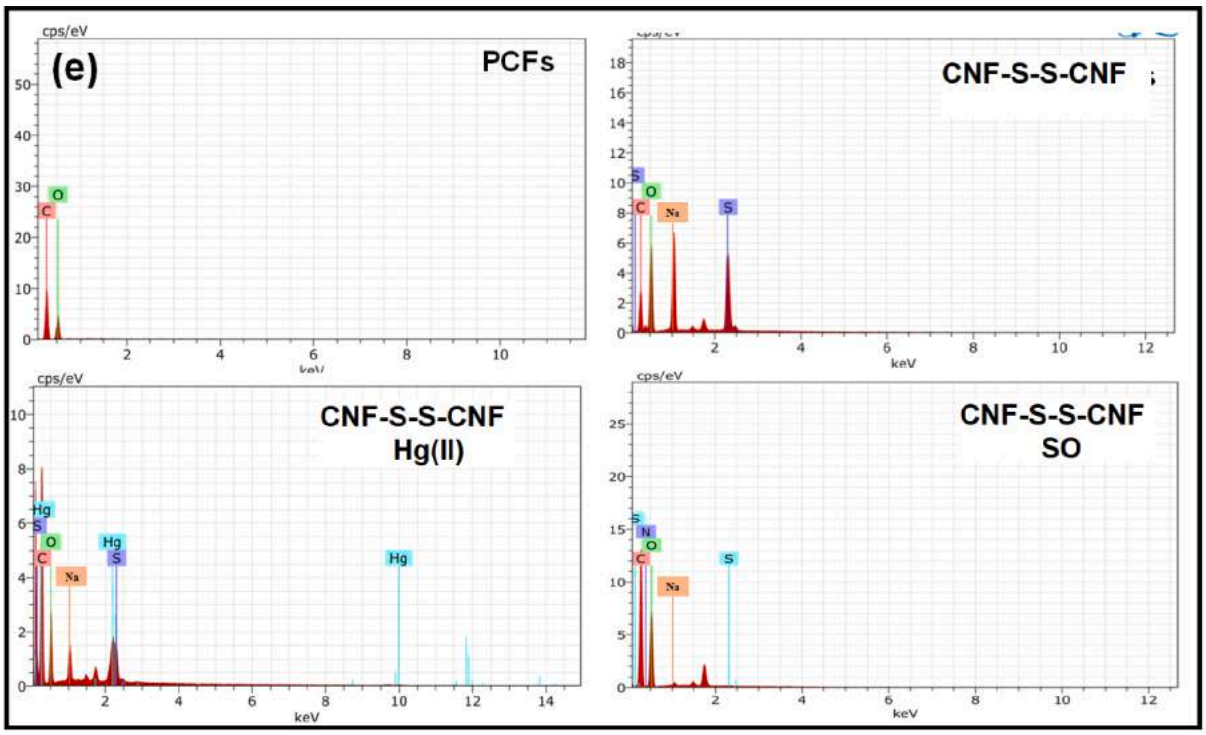

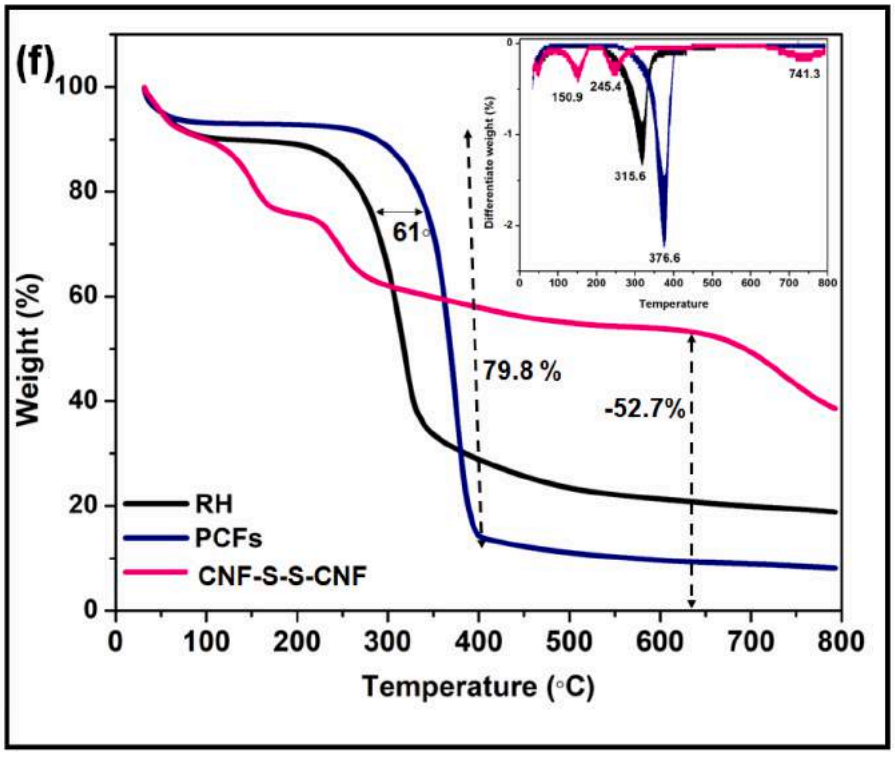

Fig. 2. (*continued*).

Fig. 2(c) gives the HRTEM micrographs of PCFs (i and ii) and CNF-S-S-CNF at different magnifications. PCFs are seen as entangled and agglomerated nanofibrous bundles of 30–50 nm, with smooth surface free from amorphous domains of lignin and hemicellulose. CNF-S-S-CNF (Fig. 3 (iii & iv)) seems to have a thin coating on the surface of fibres almost with similar diameter as PCFs. The tendency of agglomeration is seemingly reduced with functionalization, however the fibres are smaller in length with 60–70 nm diameter. Fig. 2(d) exhibits FESEM images of pristine cellulose fibres (i and ii), and the morphology of CNF-S-S-CNF is shown in Fig. 2d (iii and iv). While the PCFs are visible as distinct fibres, CNF-S-S-CNF appears to be a porous network constituted of fibrous mass. The network aids in quicker penetration of analyte molecules into the inner space and provides a large number of ion-coordinating sites conducive for adsorption. Closer representation exhibits (Fig. 2d (iv) inset) significantly decreased aspect ratio with functionalization, as confirmed by TEM. This probably is due to

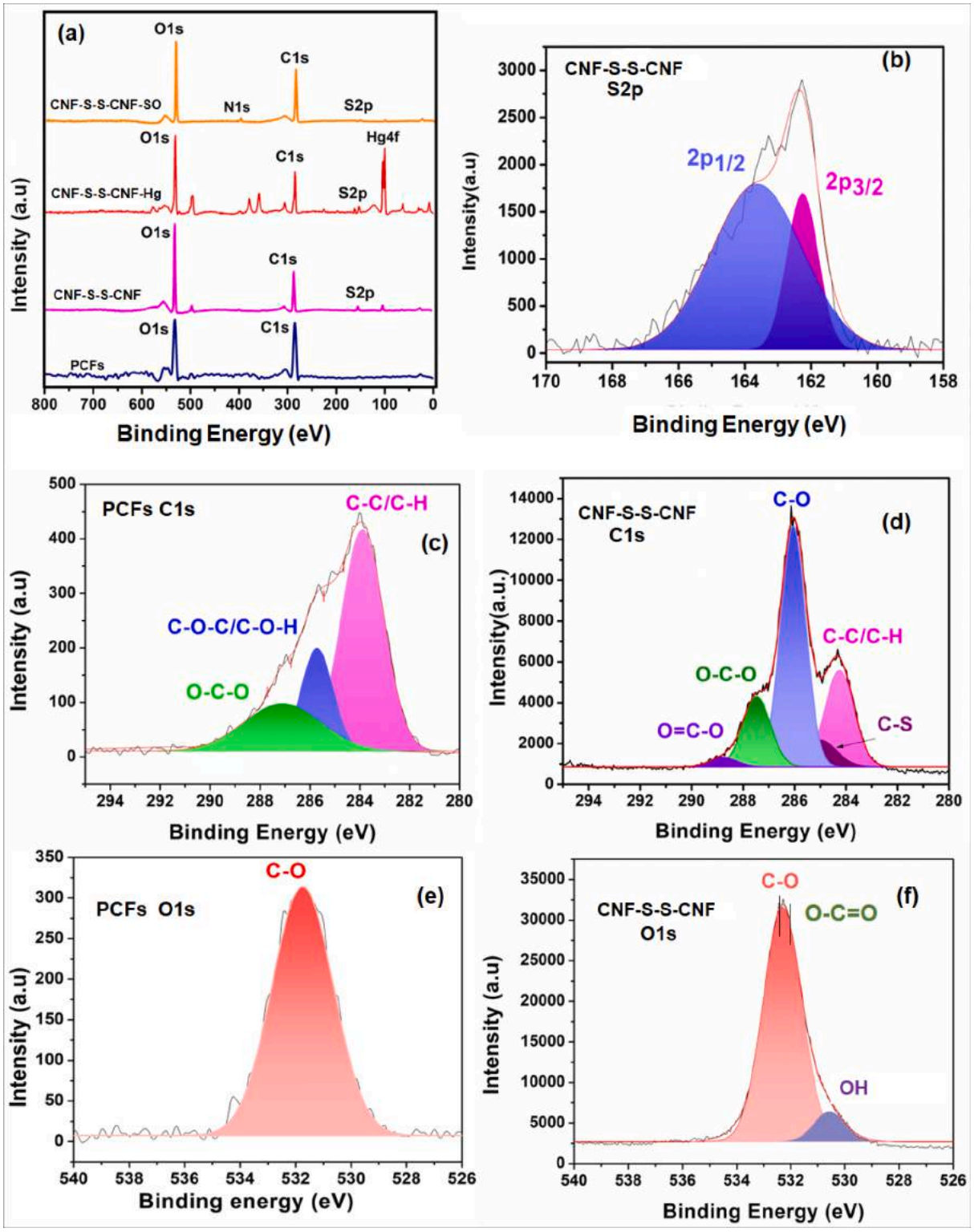

Fig. 3. XPS analysis of pristine cellulose fibres (PCFs) and CNF-S-S-CNF.

regeneration process of cellulose during functionalisation. This is also corroborated by the thermal analysis of PCFs and CNF-S-S-CNF which reveals a lower onset of degradation post-functionalization.

The energy dispersive X-ray (EDX) results of PCFs, CNF-S-S-CNF and adsorbent loaded with Hg(II) and SO have been presented in Fig. 2(e). PCFs clearly show the presence of only carbon and oxygen constituting the backbone of biomass. The DTPA modified cellulose fibres visibly show the presence of sulphur due to presence of disulphide group. Presence of Hg(II) ions and nitrogen confirms the adsorption of Hg(II) and SO on the surface of CNF-S-S-CNF.

Thermal analysis of RH, PCFs and CNF-S-S-CNF was studied to evaluate the effect of functionalization on their thermal behaviour as illustrated in Fig. 2(f) and differential thermogravimetric (DTG) analysis (inset). The peak decomposition of RH occurs at 315.6 °C, while for PCFs a sharp degradation ensues at 376.6 °C i.e. 61 °C higher than RH, clearly demonstrating the high purity of cellulose due to removal of

hemicellulose and lignin in PCFs. It is worth mentioning that at temperature below 100∘C, all samples showed a small weight loss (≈ 10%), attributable to the removal of absorbed water onto the surface. As evident from the thermogram, PCFs are thermally most stable because of their ordered crystalline structure with onset degradation temperature of 235.4∘C and maximum degradation 376.6∘C (mass loss 79.8% at 700 °C), which is due to the degradation of β(1–4) glycosidic linkages translating into carbon dioxide (CO_2), carbon monoxide (CO) and methane (CH_4) gasses. Unlike PCFs which exhibit a single sharp degradation peak, CNF-S-S-CNF degrades in multiple steps [48]. The onset of degradation occurred at a lower temperature of 215.5∘C which is due disruption of its crystalline structure during regeneration and introduction of functional groups in the backbone of cellulose. The peak degradation occurs at 245.4∘C, probably due to the initial stage of breakdown of ester bonds in CNF-S-S-CNF. Thereafter, sulfate half esters are formed on the surface of PCFs which combine with the water and are removed as by-products during pyrolysis to produce acids. These acids further catalyse the de-esterification, depolymerization and degradation of cellulose chains. As evident from Fig. 2(f), PCFs have higher stability and sharp degradation resulting in small volatile molecules instead of forming char, eventually resulting in low residual mass (8.8%). On the other hand, CNF-S-S-CNF with low thermal stability followed by slow pyrolysis got converted to char which provided more thermal stability up to 740∘C (52.7% residue) [49].

3.3. Xps analysis

The CNF-S-S-CNF was further characterized using XPS spectroscopy, which is a sensitive surface characterization technique with a sampling depth of 10 nm. The results of XPS are given in Fig. 3. Fig. 3a shows the wide XPS survey of PCFs and CNF-S-S-CNF, while Fig. 3c and 3d exhibit the C1s spectra. Fig. 3e and 3f display the O1s spectra of PCFs and CNF-S-S-CNF, respectively, while S_{2p} spectra for CNF-S-S-CNF is shown in Fig. 3b. The appearance of new peak for S_{2p} in the XPS spectra of CNF-S-S-CNF confirms the successful grafting of disulphide linkage on the surface of PCFs. The S_{2p} spectra were deconvoluted into two peaks, the first peak appearing at 162.20 eV for $2p_{3/2}$ and the other peak visible at 163.3 eV for $2p_{1/2}$, which correspond to disulphide linkages on the surface of the CNF-S-S-CNF [50]. In the deconvoluted C1s XPS spectra of PCFs, three peaks appeared at 284.00 eV (C–C/C–H), 285.65 eV (C-O-C/C-O–H) and 287.7 eV, confirming that (O-C-O) linkages are present in PCFs [38]. In the C1s spectra of CNF-S-S-CNF, two new peaks appeared, which correspond to C-S linkages at 285.0 eV and O = C-O linkages at 288.0 eV, which also corroborates the FTIR results. In the PCFs, a single peak is formed at 531.6 eV which is attributed to C-O linkage, while the O1s spectrum of CNF-S-S-CNF displayed two split peaks appearing at 532.2 eV and 532.4 eV, which correspond to O-C = O and C-O bonds in DTPA, respectively [38].

3.4. Model establishment and analysis of process parameters for the adsorption of Hg(II) and SO on the surface of CNF-S-S-CNF

The RSM based BBD approach was utilized to determine the impact of independent variables i.e. pH (A), contact time (B), initial concentration (C), and adsorbent dosage (D) on the adsorption of Hg(II) and SO. Table S2a and Table S2b, section S5 (supplementary file) display the core composite matrix and the outcomes of total 29 randomized tests for Hg(II) and SO, respectively. The 3D response surfaces were drawn using the model. Based on the results of the experiments of variables (given in table S2a and table S2b), the proposed quadratic expressions developed between adsorption rate and testing parameters are illustrated in equations (21) and (22).

Response (Hg(II) adsorption)

$$=77.50+8.26A+19.15B-26.03C+13.44D+6.30AB+6.63AC+1.65AD+15.75BC+8.00BD+12.73CD-16.47A^2-16.01B^2+11.79C^2-15.15D^2 \quad (21)$$

Response (SO adsorption)

$$=62.35+21.28A+1.08B-6.86C+10.04D+12.25AB-11.65AC+2.33AD+5.66BC+8.82BD+10.62CD-11.38A^2-0.77B^2+3.32C^2-6.59D^2 \quad (22)$$

where, A, B, C and D denote the experimental parameters i.e. pH, contact time, adsorbate concentration and adsorbent dosage, respectively. Whereas, the negative and positive signs of the coefficients in the equations denote antagonistic and synergistic effects, respectively.

The summary of the results of the analysis of variance (ANOVA) for the quadratic model which includes the sum of squares (SS), degree of freedom (df), mean squares, F-value and probability > F values for each element is given in table S3a and table S3b for Hg(II) and SO, respectively. The model F-value of 13.47 for Hg(II) and 54.22 for SO implies that the model is significant. There is only a 0.01 % chance that an F-value this large could occur due to noise. A P-value<0.0500 indicate model terms are significant. In the case of Hg(II), A, B, C, D, BC, CD, A^2, B^2, C^2 and D^2 are the significant model terms, While SO, A, C, D, AB, AC, BC, BD, CD, A^2 and D^2 are the significant model terms. Besides, the coefficient of determination (R^2), predicted (R^2_{pre}) and adjusted (R^2_{adj}) were statistical measures used to determine the significance and sufficiency of the suggested model. The R^2 value closer to 1 implies the significance of the model. The value of R^2, R^2_{adj} and R^2_{pre} are given in **Table S4** (i.e. for Hg(II) $R^2 = 0.9309$, $R^2_{adj} = 0.8618$ and $R^2_{pre} = 0.6964$ and for SO $R^2 = 0.98$, $R^2_{adj} = 0.93$ and $R^2_{pre} = 0.86$), also validate the results. Adequate precision measures the signal to noise ratio. A ratio>4 is desirable. The adequate ratio 11.21 for Hg(II) and 29.43 for SO indicate an adequate signal. The two-dimensional (2D) and three-dimensional (3D) response surfaces are shown in Fig. 4 and the

Table 2
Kinetic parameters for linear pseudo first order and pseudo second order models.

Pollutant	Conc. (mgL^{-1})	Pseudo first order kinetics					Pseudo second order kinetics			
		$q_{e,\ exp}$ ($mg.g)^{-1}$	K_1 (min^{-1})	$q_{e,\ calculated}$ ($mg\ g^{-1}$)	R^2	$R^2_{adj.}$	K_2 ($g\ mg^{-1}\ min^{-1}$)	$q_{e,\ cal}$ ($mg\ g^{-1}$)	R^2	$R^2_{adj.}$
Hg(II)	10	9.97	0.72	2.33	0.9563	0.8303	68.5	10.1	0.9994	0.9985
	100	99.30	0.55	167.04	0.9565	0.8933	1.2×10^{-3}	117.78	0.9912	0.9796
	200	181.86	0.34	208.98	0.9873	0.9711	6.2×10^{-4}	218.34	0.9623	0.9841
	400	348.6	0.36	772.87	0.8978	0.7784	1.6×10^{-4}	510.20	0.9950	0.9138
	600	530.8	0.19	523.95	0.9799	0.9536	1.1×10^{-4}	757.57	0.9977	0.9888
	800	735.9	0.34	641.60	0.9449	0.8666	0.87×10^{-4}	1022.4	0.9958	0.9947
	1000	828.5	0.24	515.03	0.9578	0.8968	0.76×10^{-4}	1150.7	0.9958	0.9902
SO	5	4.42	0.33	4.09	0.9525	0.9434	0.313	4.55	0.9996	0.9991
	10	8.65	0.22	6.28	0.9676	0.9496	0.114	8.95	0.9995	0.9990
	15	12.78	0.17	7.74	0.9483	0.9233	0.069	13.18	0.9994	0.9987
	20	16.75	0.26	17.02	0.9762	0.9652	0.44	17.67	0.9995	0.9990
	30	21.48	0.27	20.67	0.9681	0.9593	0.041	21.00	0.9997	0.9995

Table 3
Kinetic parameters for non-linear pseudo first order and pseudo second order models.

		NL-PFO					NL-PSO			
Pollutant	Conc. (mgL^{-1})	$q_{e,\ exp}$ ($mg\ g^{-1}$)	K_1 (min^{-1})	$q_{e,\ cal.}$ ($mg\ g^{-1}$)	R^2	$R^2_{adj.}$	K_2 ($g\ mg^{-1}\ min^{-1}$)	$q_{e,\ cal.}$ ($mg\ g^{-1}$)	R^2	$R^2_{adj.}$
Hg(II)	10	9.97	0.80	9.4	0.9921	0.9955	0.19769	10.32	0.9955	0.9982
	100	99.30	0.42	96.09	0.9960	0.9961	0.00681	108.39	0.9977	0.9964
	200	181.86	0.22	145.49	0.9876	0.9834	0.00119	223.60	0.9953	0.9911
	400	348.6	0.18	305.28	0.988	0.984	3.9×10^{-4}	463.45	0.9990	0.9780
	600	530.8	0.21	422.56	0.9755	0.9712	4.1×10^{-4}	628.97	0.9990	0.9869
	800	735.9	0.27	669.32	0.9570	0.9476	4.6×10^{-4}	810.79	0.9887	0.9757
	1000	828.0	0.31	767.32	0.9345	0.9288	5.1×10^{-4}	877.23	0.9975	0.9916
SO	5	4.42	0.53	4.29	0.9841	0.9781	0.22654	4.60	0.9962	0.9832
	10	8.65	0.42	8.34	0.9855	0.9654	0.07746	9.14	0.9976	0.9721
	15	12.78	0.38	12.22	0.9851	0.9763	0.0463	13.51	0.9979	0.9812
	20	16.75	0.31	16.42	0.9872	0.9785	0.0252	18.54	0.9977	0.9851
	30	21.48	0.35	22.47	0.9888	0.654	0.02423	23.36	0.9988	0.9835

detailed discussion on the optimization of parameters based on these figures is mentioned in Section S5 (section b), supplementary file.

It was established from the results that the maximum adsorption capacity i.e. 100% removal of 100 mL of 10 mg L^{-1} of Hg(II) ions was achieved at pH 5.5 with two combinations i.e. contact time of 9.50 min and CNF-S-S-CNF dosage of 100 mg and second with 18 min contact time and 60 mg CNF-S-S-CNF dosage, while complete removal of 100 mL of 1 mg L^{-1} of SO was accomplished at optimum conditions of pH 6.5, CNF-S-S-CNF dosage of 60 mg and contact time of 9.50 min. These results obtained from RSM were validated using experimental parametric studies.

3.5. Experimental adsorption parameters

The adsorption was investigated as a function of parameters used for RSM i.e contact time between adsorbate and adsorbent, the concentration of adsorbate and adsorbent, and the effect of the pH of the medium and interference of other metal ions. At different time intervals of the adsorption process, the adsorption percentage and adsorption capacities were evaluated using equations (3) and (4).

3.5.1. Point of zero charge (PZC)

ZPC is the pH where the net charge density on the surface of the adsorbent is zero. The graph of $\Delta pH = pH_{Final}\text{-}pH_{Initial}$ is shown in Fig. 5 (a). As evident, the ZPC value of CNF-S-S-CNF is 4.6. After 24 h, all the adsorbent solutions with different pH values equilibrate at pH-4.6, below which, the adsorbent surface has a net positive charge and above, a net negative charge.

3.5.2. Selectivity of metal ions and textile dye

For practical applications, target ions do not exist but they typically coexist with competing metal ions. To ascertain the selectivity of CNF-S-S-CNF towards Hg(II) ions, competitive adsorption with interfering cations was conducted with alkali metal ions like K(I), Na(I) and heavy metal ions such as Pb(II), Co(II), Cu(II), Fe(II), Cd(II) and Cr(III). Since Hg(II) and sulphide are soft acids and soft bases, respectively, it was postulated that Hg(II) ions have stronger attraction towards the disulphide group as compared to other metal ions. As hypothesized, the removal efficiency and uptake kinetics of Hg(II) ions were much higher than other metal ions (Fig. 5(b)), confirming a high selectivity for Hg(II). Almost 100% removal of Hg(II) ions was achieved in initial 5 s for C_o = 10 mg L^{-1} *(as is evident in the attached videos)*. As mentioned in section 2.5.2, TMK was used to make complex with Hg(II) for spectroscopic detection. TMK gives a light-yellow colour in a slightly acidic medium (i.e. pH 5.5 at which the adsorption of Hg(II) ions is maximum) and forms a blue-purple coloured complex with mercury ions in an aqueous medium. *In the video, the colour change from blue to yellow is evident, which establishes the adsorption of Hg(II) ions on CNF-S-S-CNF.*

For other metal ions i.e. Pb(II), Co(II), Cu(II), Fe(II), Cd(II) and Cr(III), even after a contact period of 2 h, the removal efficiencies were very low i.e. 13.4%, 3.87%, 4.87%, 5.13%, 3.87% and 3.43%, respectively (Fig. 5(b)), clearly indicating a high selectivity of Hg(II) ions. A low percentage of alkali metal ions, Na(I) and K(I) ions was captured i.e. 3.23 % and 2.9 %. Additionally, as dissolved organic matter (DOM) is normally present in an actual wastewater environment, the antifouling of the adsorbent is crucial for the removal of ionic species. Humic acid (HA) was used as a representative DOM to assess its impact on removal of Hg(II) by CNF-S-S-CNF. HA was removed to about 3.5 % implying that presence of HA in water has negligible influence on the adsorption of Hg (II) ions (Fig. 5(b)).

It is essential to assess the selectivity of adsorbent for various metal ions. A high distribution coefficient, K_d value means higher selectivity of adsorbent towards the target ions. It is evident from Fig. S2(a) that the K_d value of CNF-S-S-CNF for Hg(II) ions is extraordinarily high i.e. 5.0×10^5 ($mL\ g^{-1}$), which is much higher than the previously reported adsorbant [51]. Further, the selectivity coefficient, $K_{Hg/M}$ was also calculated which evaluates the ability of CNF-S-S-CNF to differentiate Hg(II) from additional metal ions. From Fig. S2(b), it is evident that the $K_{Hg/M}$ values for other metal ions were in the range of 4.2×10^3–1.7×10^4, suggesting the outstanding selectivity of Hg(II) over other metal ions [52].

CNF-S-S-CNF was also evaluated for removal of textile effluents, Safranin O (SO). SO being a cationic dye, the resultant strong electrostatic force of attraction between negatively charged adsorbent and positively charged dye is responsible for its adsorption on CNF-S-S-CNF. It was observed that CNF-S-S-CNF exhibited good selectivity for SO for broad concentration range, hence the parametric studies were accomplished for both, Hg(II) ions and SO dye.

3.5.3. Effect of time and equilibrium

The contact time between adsorbent and adsorbate is important in deciding the adsorption performance. The concentration changes in Hg (II) and SO w.r.t. time were evaluated at their maximum absorption wavelengths. Figure S3 (a and b), section S7 shows the UV graph for the adsorption of Hg(II) ions and SO dye on 100 mg of adsorbent (100 mg L^{-1} solution of Hg(II) ions at pH-5.5 and for 5 mg L^{-1} solution of SO dye pH −6.5). The studies were accomplished with time ranging from 0 to 120 min. The equilibrium was attained within 8 min in the case of Hg(II) (concentration of 100 mg L^{-1}) and 18 min for SO (concentration of 25 mg L^{-1}). The percentage adsorption at equilibrium for Hg(II) and SO was estimated to be 99.3 % and 88.4 %, respectively. The adsorption curves make it quite apparent that the kinetics of adsorption is distinct and rapid. Within the initial 2 min on addition of CNF-S-S-CNF, adsorption of Hg(II) reached 93.7%, while for SO it was 71.1%.

Similarly, the percentage adsorption of Hg(II) (adsorbent dosage of 100 mg, Hg(II) concentration ranging from 100 to 500 mg L^{-1}, pH-6) and

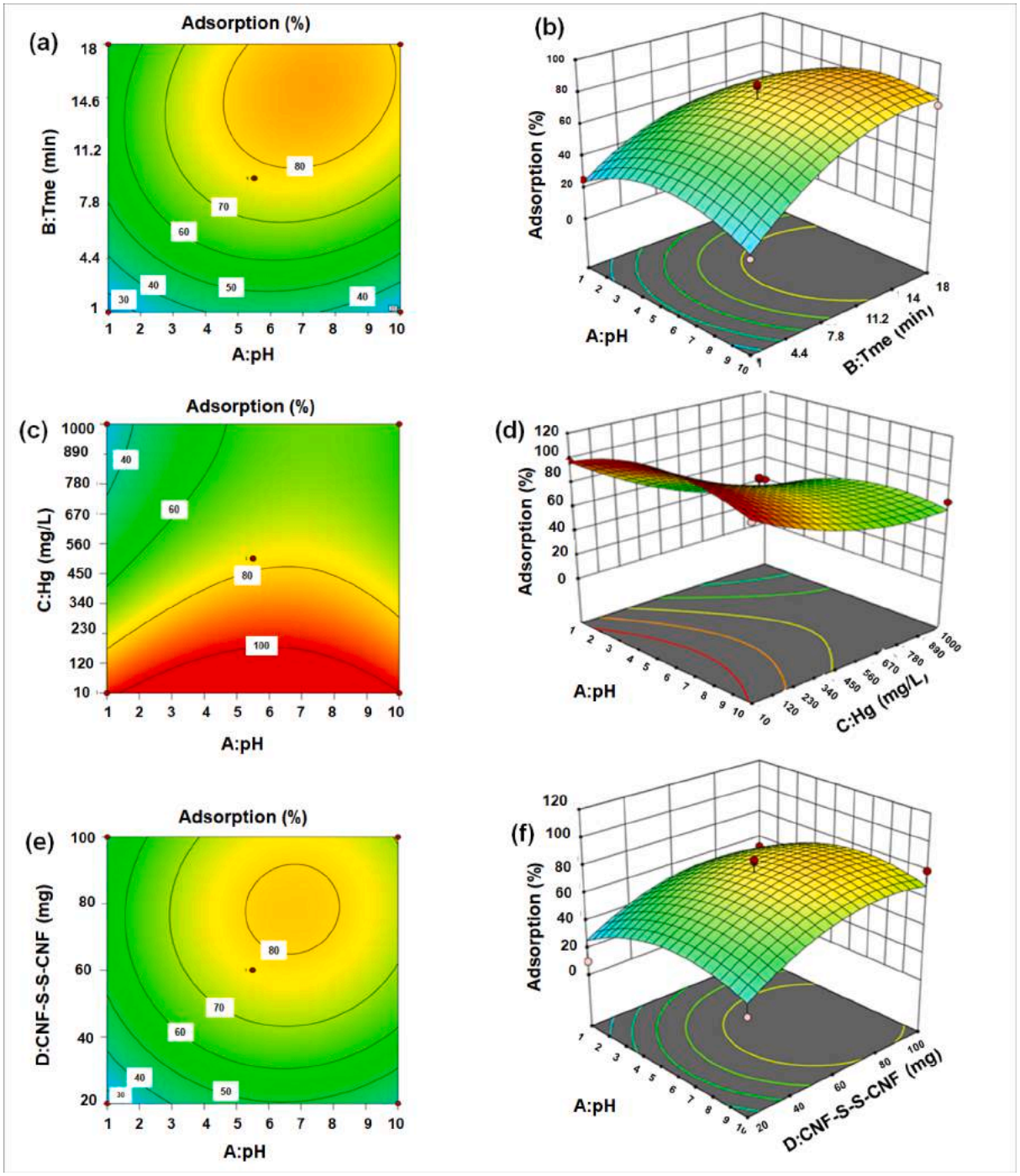

Fig. 4. Two dimensional (2D) and three dimensional (3D) response surfaces for Hg(II) and SO dye, respectively.

SO (adsorbent dosage of 100 mg, SO dye concentration 5–25 mg L^{-1}, pH-7), respectively was determined within the time interval of 0–120 min. The adsorption curves make it fairly clear that the kinetics can be divided into two distinct phases. Initially, the quick adsorption phase occurred within 2 min for Hg(II) and 3 min for SO. In this phase, about 55–97.3 % adsorption was found for metal ions concentration ranging from 500 to 100 mg L^{-1} and 55.8–71.8 % for SO with concentration varying from 25 to 5 mg L^{-1}, respectively (Fig. 5(c and d)). The faster phase significantly contributes to the equilibrium adsorption and the second, slower phase, during which the adsorption is largely insignificant lasts from 2 to 15 min for Hg(II) ions and 3 to 18 min for SO dye. In the beginning stage of the process, the concentration gradient is significantly high and there are a lot of easily accessible binding sites, however, as time proceeds, both of these factors decline and the process slows down as equilibrium is reached.

3.5.4. *Effect of pH of medium*

The pH of the system not only affects the existence of different ionic forms of Hg(II) species but also influences the surface properties of the adsorbent. From Fig. 5 (e and f), it is evident that CNF-S-S-CNF has low removal capacity for Hg(II) ions at lower pH values i.e. in the range 1–3 (i.e. 55%-70%), however as pH increased from 4 to 7, CNF-S-S-CNF exhibited a higher adsorption capacity (84%-98%). The adsorption decreased when pH was further increased from 8 to 12 (<70%). This can

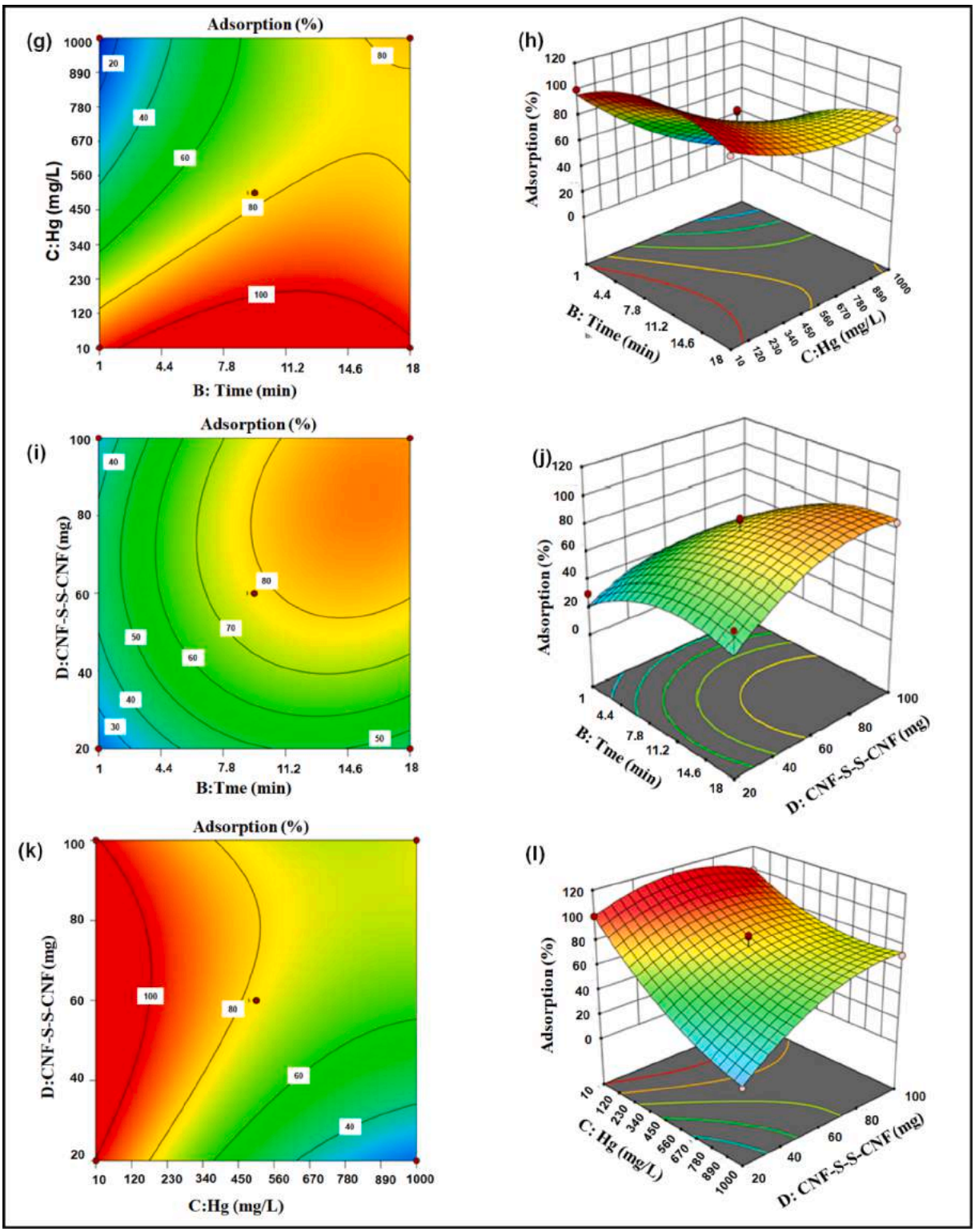

Fig. 4. (*continued*).

be explained as under different pH conditions, mercury exists in different ionic forms including Hg(II), Hg $(OH)^{+}$, Hg (OH) etc. in the aqueous system. At low pH i.e. pH < 4, Hg (II) ions exist, however, they compete with ions which have smaller size and mobility, for adsorption leading to their smaller adsorption percentage. At moderate pH i.e pH 4–6, most of the mercury is present as Hg(II) ions and small traces of Hg $(OH)_2$, which has strong electrostatic forces of attraction towards negatively charged adsorbent. CNF-S-S-CNF has a net zero-point charge at pH 4.6 (isoelectronic point), thus it exhibits an overall positive charge below pH-4.6 and negative charge above this pH. Between pH 4 to 6, negatively charged CNF-S-S-CNF displayed a strong electrostatic force of attraction towards positively charged Hg(II), increasing the adsorption. This result is in agreement with the previous reported disulfide and thiol functionalized lanthanide coordination polymers [53]. On the other hand, between pH 6–7, mercury is present in the form $Hg(OH)^{+}$, Hg $(OH)^{3+}$ and traces of $Hg(OH)_2$ which hinder the adsorption. However,

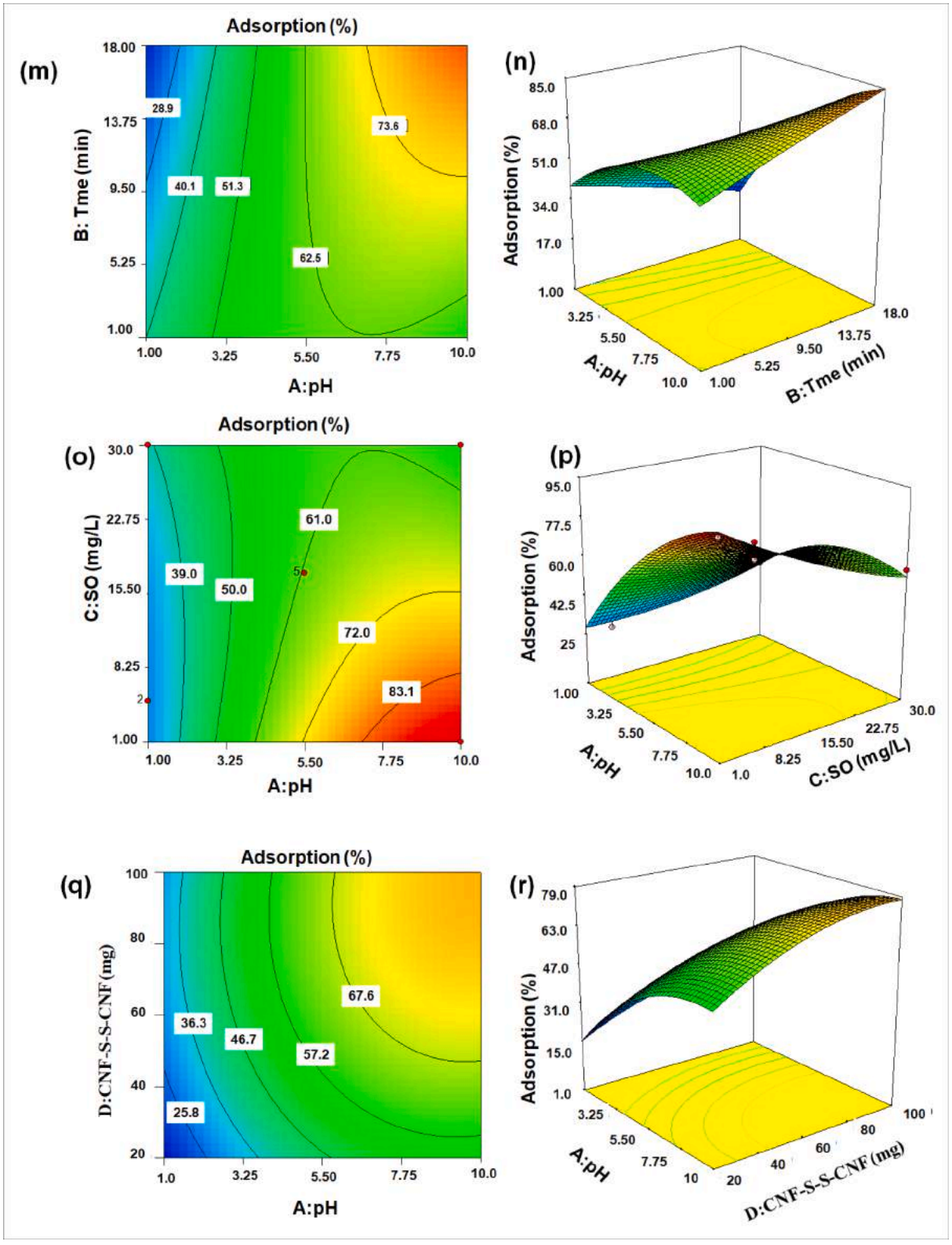

Fig. 4. (*continued*).

due to the strong negative charge on the surface of CNF-S-S-CNF, a slight decrease is observed in percentage removal capacity. After this i.e. pH 8, mercury exists as $Hg(OH)_2$ which gets precipitated in an alkaline medium, decreasing the Hg(II) removal [54].

A similar trend was observed for the adsorption of SO dye on CNF-S-S-CNF surface. At low pH, the competition between H^+ and SO cationic dye, as well as repulsion with the positively charged surface of CNF-S-S-CNF, resulted in smaller adsorption percentage of SO, however, as the pH increased above 4, the CNF-S-S-CNF has a net negative surface charge which ensues strong electrostatic forces of attraction towards the cationic dye. Hence, adsorption increases as pH increases beyond pH 4 and up to pH 8. Further increase in pH above 8, causes a slight decrease

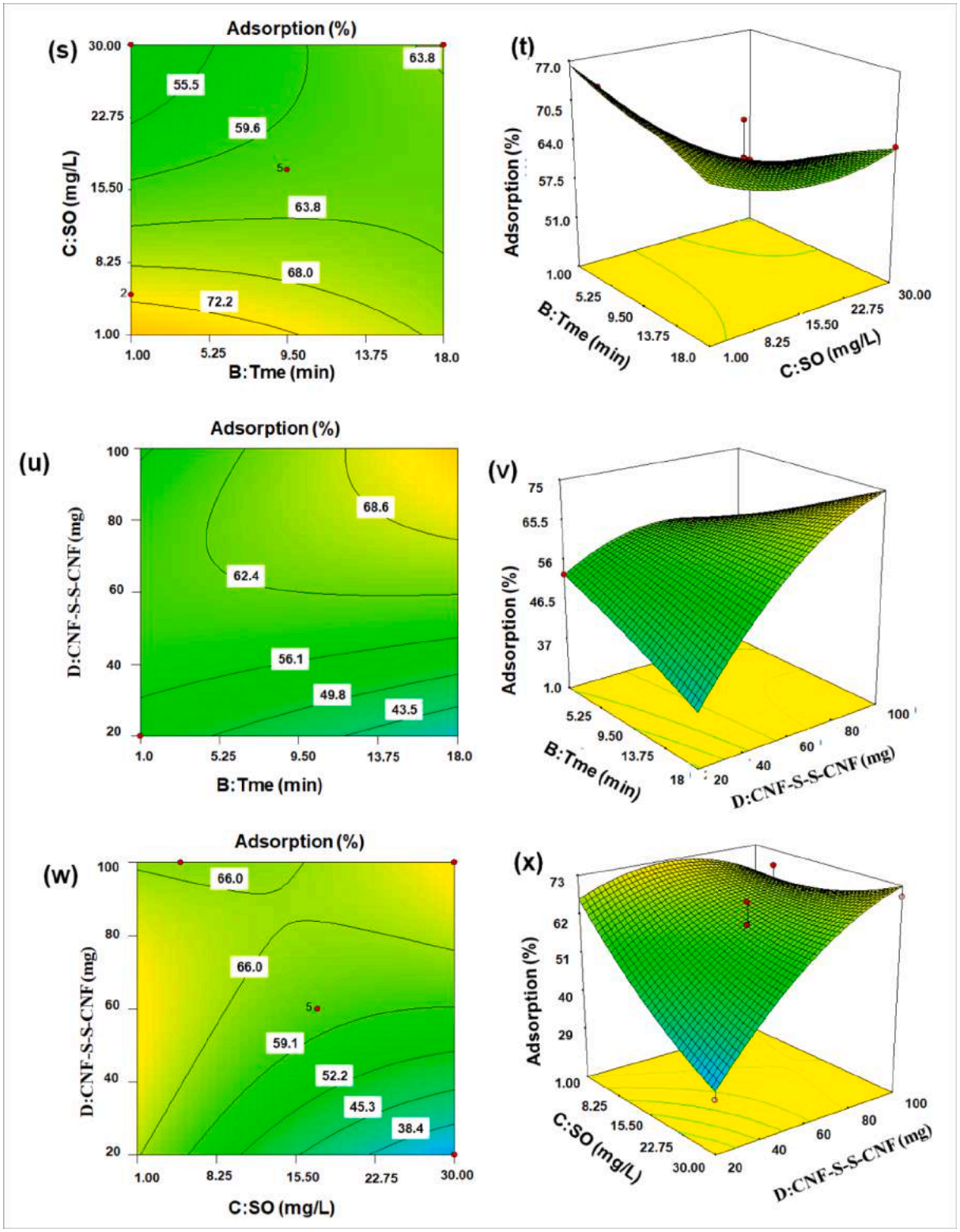

Fig. 4. (*continued*).

in adsorption. It might be due to the interference that arises between negatively charged adsorbent and hydroxyl ions in the alkali medium [55].

3.5.5. *Effect of adsorbent and adsorbate concentration*

The increase in initial metal ions concentration significantly increases the adsorption rates as it provides the necessary driving force to overcome the mass transfer resistance. To establish the optimum concentration of Hg(II) and SO and their maximum uptake capacity, experiments were performed with varying adsorbate concentrations (Fig. 5 (g and h)). The Hg(II) concentration was varied from 100 to 500 mg L^{-1} (CNF-S-S-CNF dosage 100 mg in 100 mL, pH 5.5) while SO was varied between 5 and 25 mg L^{-1} (CNF-S-S-CNF dosage 100 mg in 100 mL, pH 6.5). At low Hg(II) ion concentration i.e. 100 mg L^{-1}, 99.3% removal was

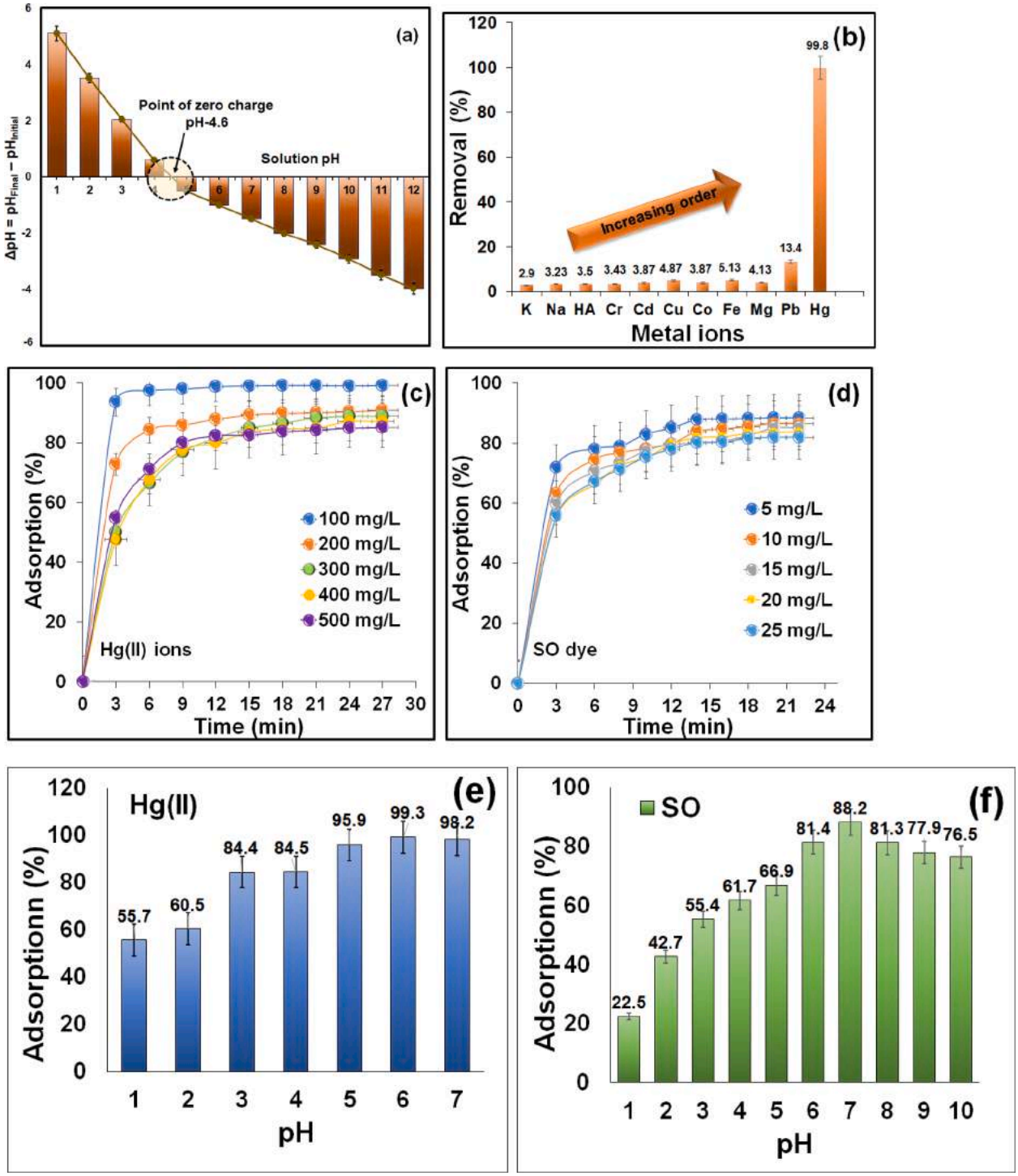

Fig. 5. (a) Point of zero charge, (b) Selectivity of CNF-S-S-CNF towards metal ions, Effect of parameters on adsorption of Hg(II) and SO (c and d) time, (e and f) pH, (g and h) initial adsorbate concentration (i and j) adsorbent concentration (with initial Hg(II) concentration of 500 mg L^{-1}, pH 6.5 for SO, initial SO concentration of 25 mg L^{-1} and pH 6.5).

achieved in 8 min observed on the surface of CNF-S-S-CNF due to the presence of abundant active sites., as shown in Fig. 5(g) and 5(h). However, as the concentration of Hg(II) ions increases to 500 mg L^{-1}, the percentage of adsorption at equilibrium decreased to 85.16% as the active sites available for adsorption get saturated. This can be elucidated as at low metal ion concentration, the ratio of metal ions to the surface active sites of CNF-S-S-CNF is large and thus the percentage adsorption is independent of metal ion concentration. However, as Hg(II) concentration increases, the accessible active sites become less as compared to existing metal ions leading to decrease in adsorption [56]. It is worthwhile to note that very few studies have reported such high concentrations of metal ions. The same tr end was observed for SO, where the percentage adsorption decreased from 88.4% to 81.92% as the concentration increased from 5 to 25 mg L^{-1}. Along with adsorbate concentration, the adsorbent dosage is an important factor to avoid excess consumption of adsorbent. The surface area accessible for the

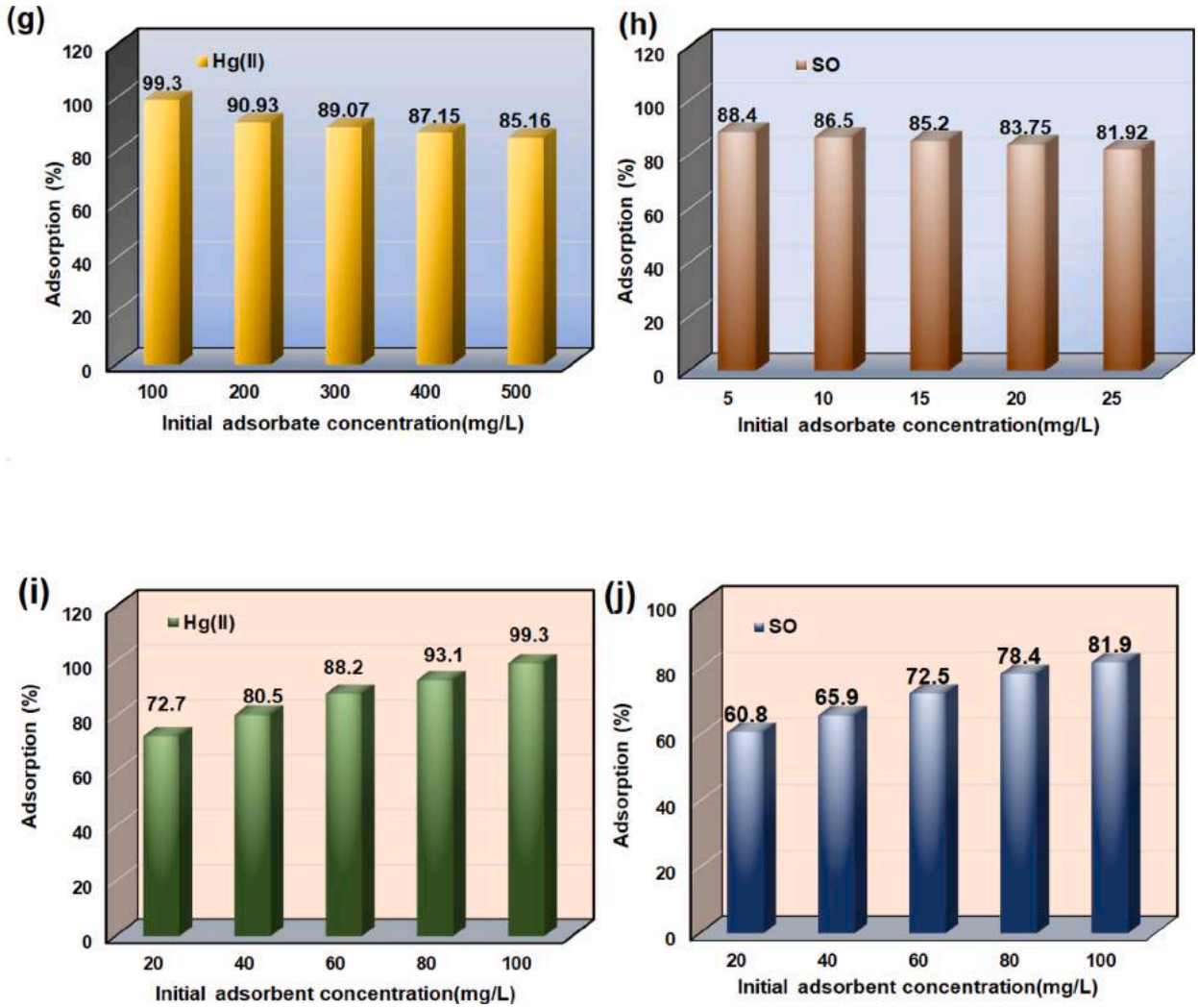

Fig. 5. (*continued*).

adsorption process increases as the amount of adsorbent increases which leads to increased number of potentially active sites. The impact of CNF-S-S-CNF concentration on Hg(II) and SO was studied with adsorbent amount ranging from 20 to 100 mg per 100 mL solution for fixed concentration of Hg(II) (500 mg L^{-1} and pH 5.5) and SO (25 mg L^{-1} and pH 6.5). As evident from Fig. 5 (i and j), the adsorption percentage increased from 72.7% to 99.3% for Hg(II), while for SO it increased from 60.8% to 81.9% when the adsorbent dosage increased from 20 mg to 100 mg per 100 mL.

The parametric studies indicate that the experimental results were in accord with the RSM studies, validating the model results. For further kinetics studies, the 100 mL of adsorbate solution of different concentrations ranging (10–1000 mg L^{-1} for Hg(II) ions and 5–30 mg L^{-1} for SO dye) were studied with optimum adsorbent dose of 100 mg and pH-5.5 for Hg(II) and pH-6.5 for SO dye.

3.6. Adsorption kinetics

To ensure the rapidness and efficacy of CNF-S-S-CNF to remove Hg (II) and SO, the linear and non-linear PFO and PSO kinetics were studied in a wide concentration range of 10 to 1000 mg L^{-1} for Hg(II) ions and 5 to 30 mg L^{-1} for SO dye. The linear and non-linear kinetic model fittings have been presented in Fig. 6, for both Hg(II) and SO, while the kinetic parameters for linear and non-linear kinetic models are given in Table 2 and Table 3, respectively. For PSO, the theoretical value of adsorption capacity ($q_{e,cal}$ = 1150.7 mg g^{-1} for linear PSO, $q_{e,cal}$ = 877.23 mg g^{-1} for NL-PSO) and experimental value at equilibrium ($q_{e,\ exp}$ = 828.5 mg g^{-1}) are closer as compared to PFO model ($q_{e,cal}$ = 515.03 mg g^{-1} for linear PFO and $q_{e,cal}$ = 767.32 mg g^{-1} for NL-PFO model) (Table 1). For SO, the experimental value ($q_{e,exp}$ = 21.48 mg g^{-1}) is closer to linear PSO model ($q_{e,cal}$ = 21.00 mg g^{-1}) as compared to NL-PSO ($q_{e,cal}$ = 23.36 mg g^{-1}), and values of error functions (table S5) conform to PSO model. Moreover, the value of correlation coefficient, $R^2 \approx 0.9958$ for Hg (II) implies that the NL-PSO model and $R^2 \approx 0.9997$ for SO implies that linear PSO model is better in representing the Hg(II) and SO adsorption on CNF-S-S-CNF. While comparing error functions, χ^2, RSS and RSME (table S5) for linear and non-linear models, it was found that adsorption of Hg(II) fitted better in NL-PSO, while SO exhibited a better fit in PSO kinetics. Considering the results, it can be inferred that chemisorption is the governing mechanism and adsorption proceeds by a chemical reaction between CNF-S-S-CNF and Hg(II) as well SO through sharing of electrons and monolayer adsorption take place on the surface of the adsorbent.

To further understand the adsorption mechanism and the factors influencing the adsorption kinetics, the experimental data were also fitted into Elovich and Weber-Morris intra-particle diffusion models (Section S8). The graphs and kinetic parameters have been presented in Figure S4 and Table S6, respectively in supplementary data file. It can be concluded that NL-PSO model best delineates the adsorption of Hg(II) and SO on CNF-S-S-CNF and adsorption is via electrostatic interactions.

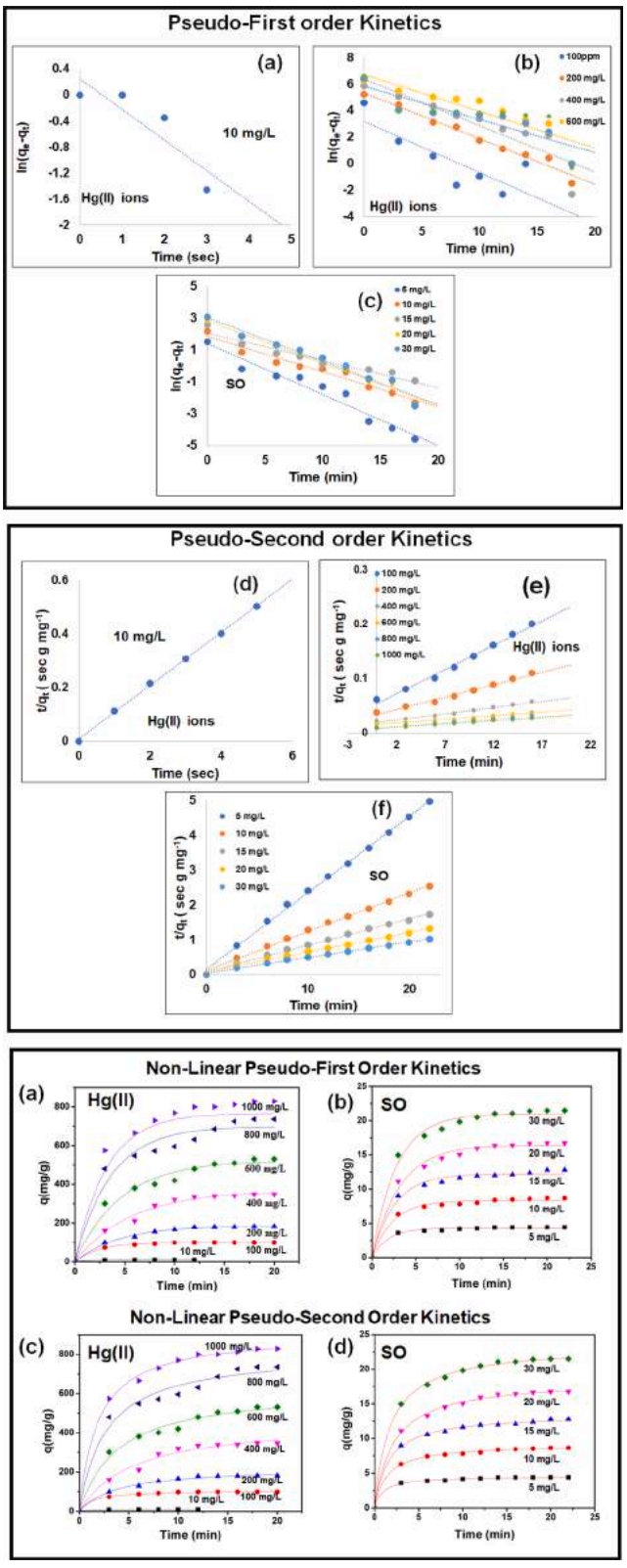

Fig. 6. Linear (a-c) pseudo-first order model, (d-f) pseudo second order model, Non-linear (g-h) pseudo first order model (i-j) pseudo-second order kinetic model (pH-6 for Hg(II) ions and pH-7 for SO dye, adsorbent dose of 100 mg).

Neither film diffusion nor intra-particle diffusion are solely the rate limiting steps, but the external mass transfer and surface adsorption also play a significant role.

3.7. Adsorption isotherm

The linear experimental fit for Langmuir and Freundlich isotherm have been plotted in Fig. 7 and the isotherm parameters are given in Table 4. The figures clearly indicate that the non-Langmuir isotherm gives a better fit than Freundlich isotherm for both, Hg(II) and SO for the experimental data with R^2 values of 0.9999 and 0.9989, respectively. When compared with non-linear models, the values of error function conform to non-linear Langmuir model for Hg(II) ions and linear Langmuir model for SO dye. The results evidently confirm chemisorption of Hg(II) on CNF-S-S-CNF and it is evident that the adsorption of Hg (II) and SO is via monolayer adsorption and both the pollutants are adhered to the adsorbent surface on evenly distributed active sites, which was confirmed by XPS results. As is evident that Freundlich isotherm does not provide a good fit for the experimental data. It is also confirmed by experimental Freundlich constant "K_F" and adsorption intensity "n" values, which are 82.5, 2.27 for Hg(II) ions and 6.51, 1.67 for SO dye, respectively, clearly indicating towards unfavourable multilayer adsorption. The favourable and unfavourable adsorption of Hg(II) ions and SO was further evaluated by the Separation factor (R_s), given by equation (22)

$$R_s = \frac{1}{1 + K_L C_0} \tag{22}$$

Where, K_L (L mg^{-1}) is the Langmuir constant and C_o is the initial pollutant concentration. The lower the value of separation factor, more favourable is the adsorption. There can be four possible cases, if $R_s = 0$, it means irreversible adsorption, $0 < R_s < 1$ indicates favourable adsorption, $R_s = 1$ is for linear adsorption and $R_s > 1$ signifies unfavourable adsorption. Since the value is lying closer to 0, it indicates favourable adsorption.

3.8. Xps analysis and adsorption mechanism

From kinetic data and adsorption isotherm, it was evident that adsorption of Hg(II) and SO on CNF-S-S-CNF occurred via chemisorption. The wide scan XPS spectra (Fig. 8), was analysed to further confirm the mechanism of adsorption. From XPS spectra, the appearance of two new peaks of Hg4f and N1s confirms the adsorption of Hg(II) and SO dye. The high resolution spectra of Hg(II) ions revealed two peaks at 100.87 eV and 105.65 eV [44]. The mechanism is governed by Hard and Soft Acids and Bases (HSAB) rule and electrostatic force of attraction at different pH values. According to the HSAB rule, "hard acids prefer to coordinate with hard bases and soft acids with soft base". Since Hg(II) and sulphide are soft acids and soft base, respectively, Hg(II) ions have strong attraction towards disulphide group [57,58]. Shifts in the peaks towards high binding energy and increase in intensity of XPS spectra of S2p ($S2p_{3/2}$ 162.2 eV, $I = 4.6 \times 10^3$ cps) and 163.3 eV ($S2p_{1/2}$, 163.3 eV, $I = 4.1 \times 10^3$ cps) to 163.0 eV ($I = 8.7 \times 10^3$ cps) and 164.1 eV ($I = 8.1 \times 10^3$ cps), respectively confirm strong electrostatic force of interaction between Hg(II) ions and disulphide bonds.

CNF-S-S-CNF has ZPC at pH of 4.6. Below pH-4.6, the adsorbent surface has a net positive charge and above a net negative charge. As pH of the solution reached 5.5, the α-hydrogen in CNF-S-S-CNF gets deprotonated to form enolate ions ensuing Hg(II) ion adsorption, which is confirmed through high resolution XPS of C1s of CNF-S-S-CNF taken after mercury adsorption [59]. The XPS spectra showed a new high intense peak of C = C at 284.2 eV (Intensity, $I = 2.1 \times 10^4$ cps), confirming the formation of double bond after deprotonation [60]. The enolate ions show electrostatic attraction towards Hg(II) ions, which results in decreased intensity of outer electrons and increase in binding energy of inner electrons of O-C-O to 287.9 eV ($I = 1.1 \times 10^4$ cps) from

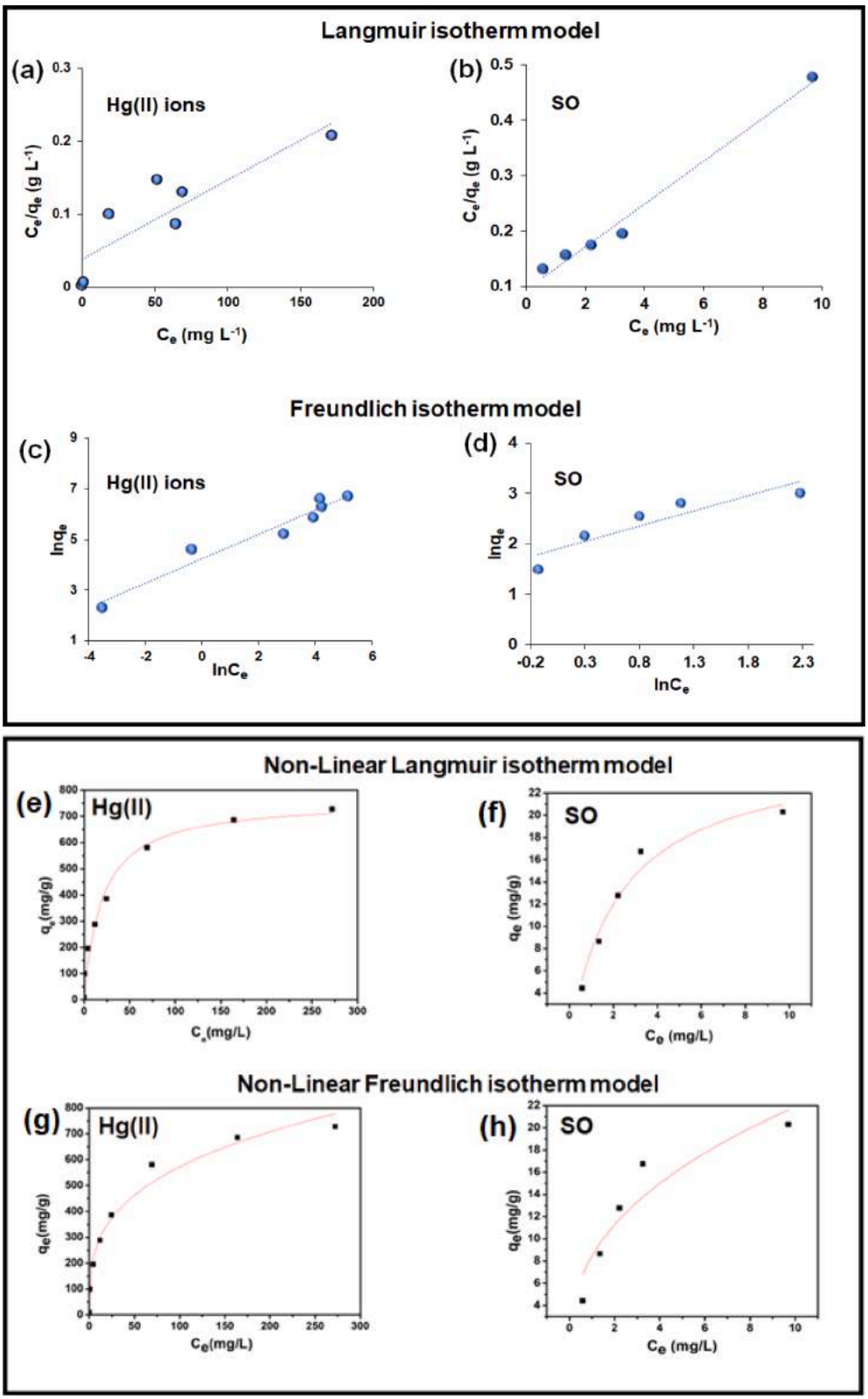

Fig. 7. Linear (a, b) Langmuir isotherm fit (c-d) Freundlich isotherm, Non-linear fit (e-f) Langmuir isotherm (g-h) Freundlich isotherm for Hg(II) ions and SO.

287.5 eV (I = 4.2 × 10^4 cps) as for CNF-S-S-CNF. The shift in the peaks and increase in intensity of C-S from 285.0 eV (I = 6.5 × 10^4 cps) to 285.2 eV (I = 1.2 × 10^4 cps) further reveals the involvement of disulphide in Hg(II) adsorption [61]. In the deconvoluted O1s spectra, O1s peak becomes broader and of higher intensity as compared to that CNF-S-S-CNF. After Hg(II) adsorption, a new peak of O-C-O at 532.9 eV (I = 3.9 × 10^4 cps) appeared in XPS spectra of CNF-S-S-CNF, confirming the conversion of O-C = O bond into O-C-O$^{\cdot}$. No change in the binding energy of C-O–H peak prior and post adsorption of Hg(II), confirmed that C-O–H of anhydroglucose units of cellulose are not involved in Hg(II) adsorption. The binding energy of O-C = O and O–H shifts to 531.7 eV (I = 3.4 × 10^4 cps) from 532.1 eV (I = 3.0 × 10^4 cps) and 530.7 eV (I = 1.8

Table 4
Isotherm parameters for various kinetic models for Hg(II) metal ions.

	Langmuir model											
Pollutants	$q_{m\ (lin)}$ (mg g^{-1})	$q_{m\ (non\text{-}lin)}$(mg g^{-1})	K_{Llin} (L mg^{-1})	$K_{L\ non\text{-}lin}$ (L mg^{-1})	R^2_{lin}	$R^2_{non\text{-}lin}$	R^2_{adjlin}	$R^2_{adj\ non\text{-}lin}$	χ^2_{lin}	$\chi^2_{non\text{-}lin}$	RSS_{lin}	$RSS_{non\text{-}lin}$
Hg (II)	1000	761.63	0.02	0.05	0.7609	0.9999	0.7549	0.9724	29.58	5.78	344	132.74
SO	25.84	26.02	0.41	0.42	0.9989	0.9888	0.9731	0.9654	0.73	1.46	8.72	9.08
Freundlich model												
Pollutants	n_{lin}	$n_{non\text{-}lin}$	K_F ((mg g^{-1})(L $mg^{-1})^{1/n}$)	K_F ((mg g^{-1})(L $mg^{-1})^{1/n}$)	R^2_{lin}	$R^2_{non\text{-}lin}$	R^2_{adjlin}	$R^2_{adj\ non\text{-}lin}$	χ^2_{lin}	$\chi^2_{non\text{-}lin}$	RSS_{lin}	$RSS_{non\text{-}lin}$
Hg(II)	2.3	0.3	82.5	139.7	0.9494	0.9774	0.9387	0.9667	1.87	1650	3.01	9.90
SO	1.7	0.4	6.5	8.5	0.9034	0.8566	0.7632	0.8454	2.87	6.00	0.25	18.01

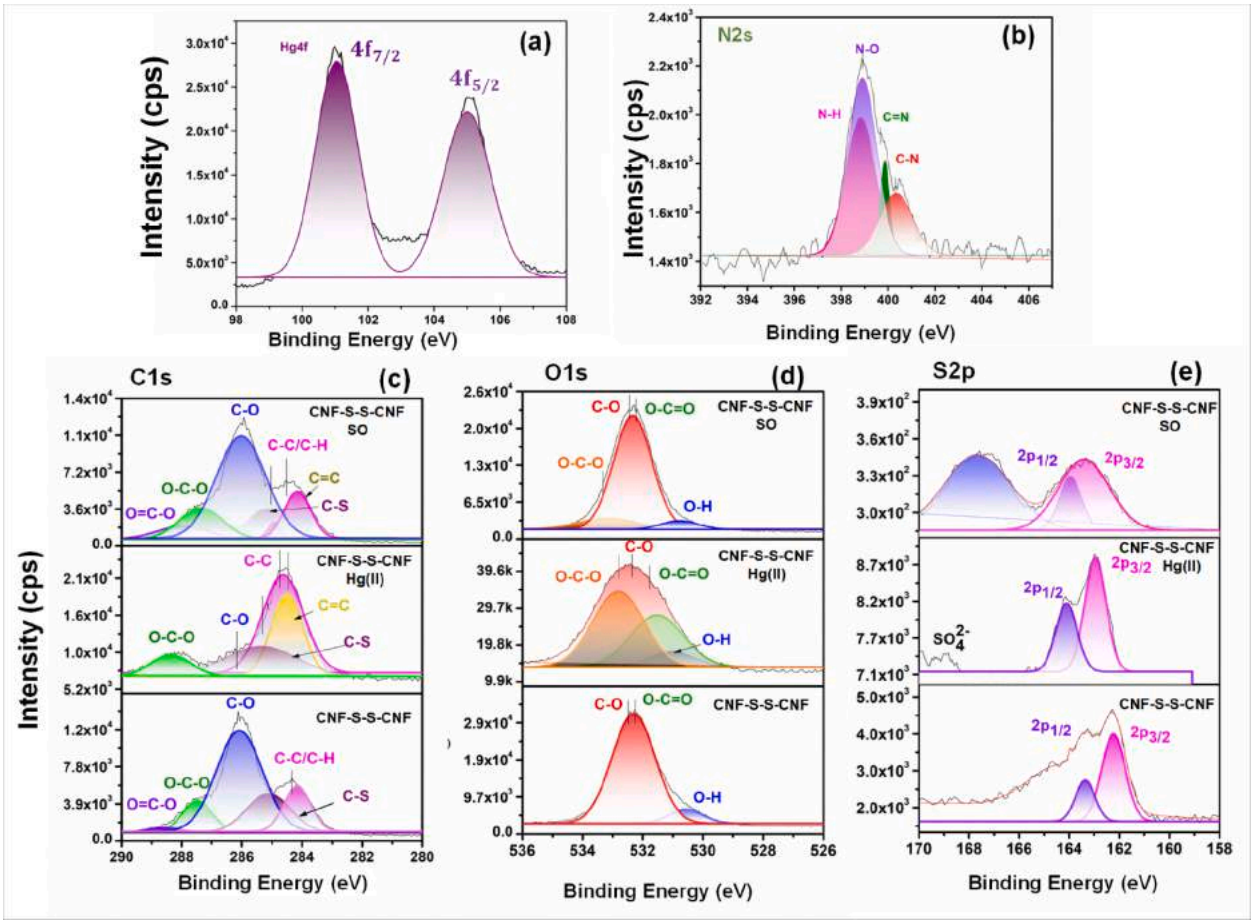

Fig. 8. XPS spectra for CNF-S-S-CNF after uptake of Hg(II) ions and SO dye.

$\times 10^4$ cps) from 530.5 eV (I = 7.7 $\times 10^4$ cps), respectively after Hg(II) adsorption [62].

On the other hand, SO being a cationic dye, the resultant strong electrostatic force of attraction between negatively charged adsorbent and positively charged dye is responsible for its adsorption on CNF-S-S-CNF. A new peak of N_{2s} appeared on the surface of CNF-S-S-CNF spectra after SO dye adsorption confirmed the adsorption of SO on the adsorbent. In the high resolution spectra of N2s, a new peak at 398.9 eV (I = 2.2 $\times 10^3$ cps) corresponds to N-O bond formation between positive charge nitrogen atom of SO and enolate ions of CNF-S-S-CNF. The other three peaks at 398.4 eV (I = 1.9 $\times 10^3$ cps), 399.6 eV (I = 1.9 $\times 10^3$ cps), 400.49 eV (I = 1.7 $\times 10^3$ cps) are attributed to the N–H, C = N and C-N bonds in SO [63]. Similarly, the binding energy of C-S, C–C, C-O, O-C-O and O = C-O in C1s spectra shifts from 285.0 eV, 284.0 eV, 286 eV, 287.5 eV and 288.0 eV to 285.1 eV, 284.4 eV, 285.9 eV, 287.8 eV, 288.1 eV, respectively. A new peak at 284.1 eV corresponds to C = C bond in CNF-S-S-CNF after SO adsorption [25,64]. In the high resolution spectra of O1s, a new peak for O-C-O appeared at 533.2 eV (I = 9.4 $\times 10^3$ cps) revealed the formation of enolate ion at high pH. The binding energy of O–H, O-C = O and C-O–H increased from 530.5 eV (I = 7.7 $\times 10^3$ cps), 532.2 eV (I = 3.0 $\times 10^4$ cps) and 532.4 eV (I = 3.1 $\times 10^4$ cps) to 530.9 eV (I = 5.288 $\times 10^4$ cps), 532.5 eV (I = 2.3 $\times 10^4$ cps) and 532.8 eV (I = 2.3 $\times 10^4$ cps), respectively. However, in the S2p spectra, the binding energy shifts from 162.2 eV (I = 4.6 $\times 10^3$ cps) to 163.3 eV (I = 3.4 $\times 10^2$ cps) for $S2p_{3/2}$ and 163.3 eV (I = 3.3 $\times 10^3$ cps) to 164.0 eV (I = 3.3 $\times 10^4$ cps) for $S2p_{1/2}$ orbital, respectively confirming that both disulphide bond has strong electrostatic force of interaction with SO. The decrease in intensity in spectra of CNF-S-S-CNF after dye adsorption might be due

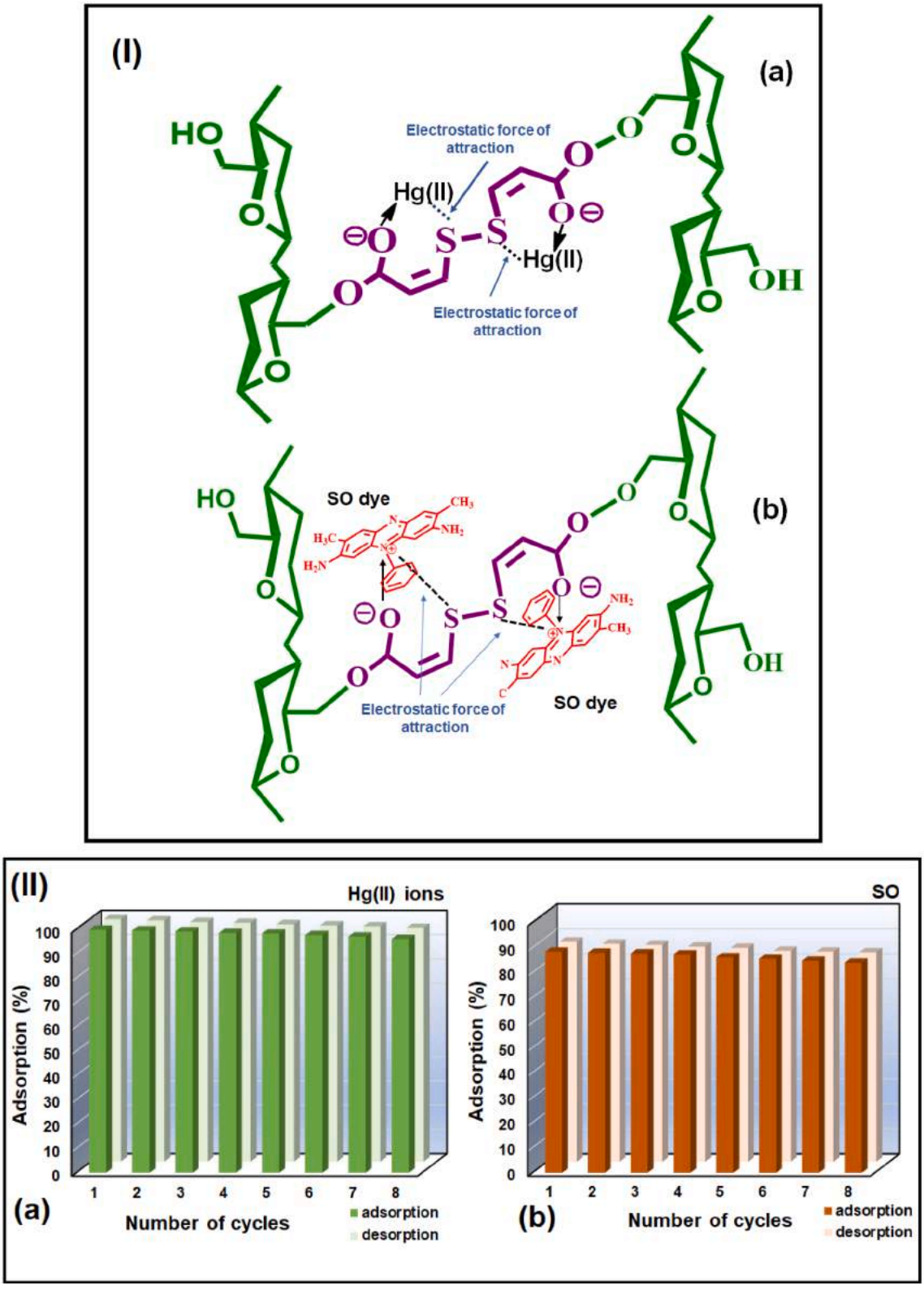

Fig. 9. (I) Adsorption mechanism (a) CNF-S-S-CNF and Hg(II) ions and (b) CNF-S-S-CNF and SO dye, (II) Reusability of CNF-S-S-CNF for Hg(II) and SO dye.

to diffusion of functional groups because of adsorbed SO on the adsorbent. The peak at 167.7 eV may be due to conversion of few sulphur atoms in disulphide bond into sulfonyl group. The EDX spectra of CNF-S-S-CNF before and after the adsorption Hg(II) and SO given in Fig. 2 (e) also substantiates the XPS results.

The adsorption mechanism *via* electrostatic interactions between the disulphide linkages of CNF-S-S-CNF and Hg(II) ions and SO dye, respectively have been elucidated in Fig. 9(I). As evident from the Fig. 9 (a) and also established from reported literature, the strong soft–soft interactions between soft acid, Hg(II) and the soft base sulphur of CNF-S-S-CNF are responsible for the adsorption of Hg(II) ions on the surface of CNF-S-S-CNF. The presence of the ester groups along with disulphide

linkages in CNF-S-S-CNF further facilitates the adsorption process through enolate ion formation at pH > 4.6. The enolate ion oxygen shows a strong electrostatic force of interaction with positive mercury ions. Similarly, strong electrostatic force of attraction between exists between cationic dye (acidic dye) and negatively charged CNF-S-S-CNF which are responsible for adsorption of SO on the surface of adsorbent, as shown in Fig. 9(b).

3.9. Regeneration and reusability

In general, regeneration ability and structural stability are the main determinants of an adsorbent's practical applicability. Strong acids like HCl are extensively employed for regeneration. However, due to strong interaction between the disulphide linkages and Hg(II), a lower acid (H^+) content fetches poor regeneration whereas higher acid concentration weakens the adsorbent structure. Consequently, using single acid is not appropriate for regeneration of CNF-S-S-CNF. Thus, 0.1% thiourea in conjunction with 0.1 M HCl was used for regeneration. As evident in Fig. 9(II), eight adsorption-regeneration cycles, the Hg(II) adsorption stayed above 96% and for SO adsorption it was above 80%. It can be thus concluded that CNF-S-S-CNF exhibits unusual potential in wastewater remediation owing to its exceptional stability and adsorption capacity after repeated cycles.

3.10. Comparison of CNF-S-S-CNF with different nanomaterials and its practical usage

The comparison of maximum adsorption capacity, equilibrium time, rate constant with various adsorbents for the removal of Hg(II) and SO reported in the literature has been presented in table S7 and table S8, respectively, while the use of CNF-S-S-CNF for adsorption of metal ions in real water analysis is given in section S9. It is evident that the performance of CNF-S-S-CNF is better than the reported materials in literature both in terms of adsorption capacity & rate constant. Thus, CNF-S-S-CNF presents a robust platform for ultra-rapid and highly efficient removal of Hg(II) and SO dye.

4. Conclusion

CNFs derived from hemp bast fibers were successfully grafted with DTPA to introduce disulphide bonds on its backbone to develop highly efficient adsorbents. The presence of disulphide groups (-S-S-) group having twice the number of sulphur atoms as compared to sulphide yielded ultra-rapid removal of Hg(II) ions with 100% removal within 5 s, not reported hitherto. FTIR, FE-SEM, TEM, TGA, XRD and XPS were used to characterize the CNF-S-S-CNF, which confirmed the regeneration of DTPA grafted CNFs, however with much lower aspect ratio as compared to PCFs. The pH, time, adsorbent dosage and initial concentration of both pollutants, Hg(II) and SO had paramount effect on adsorption on the surface of CNF-S-S-CNF and hence optimized using RSM with BBD approach. The RSM results were in close concurrence with experimental results. For Hg(II) ions, the maximum adsorption capacity was achieved at pH- 5.5, adsorbent dosage of 100 mg and contact time of 9.50 min, while for SO, the optimal conditions were, pH-6.5, CNF-S-S-CNF dosage 60 mg, and contact time of 9.50 min. Exceptional selectivity for Hg(II) can be attributed to the high K_d value of 5×10^5 mL g^{-1} in the presence of interfering metal ions. Even at very high concentration of Hg(II) ions i.e. 1000 mg L^{-1}, the equilibrium was achieved quickly within 15 min, exhibiting 82.8% removal, attributed to the porous network and hydrophilic character of CNFs. Such high concentration of Hg(II) ions has seldom been reported. The experimental data for Hg(II) ions fitted well into NL-PSO kinetic model, while adsorption of SO followed linear PSO kinetic model, which was in conformity with he reported results. Concurrence with Langmuir isotherm model and XPS studies established strong soft–soft interactions between soft acid, Hg(II) and the soft base sulphur of CNF-S-S-CNF along with the presence of ester linkages through enolate ion formation, further enhancing the electrostatic interactions. Regeneration of CNF-S-S-CNF with 0.1% thiourea and 0.1 M HCl for 8 cycles retained 96% efficacy for Hg(II) ions and 80% for SO dye, corroborating their outstanding potential in waste-water remediation.

CRediT authorship contribution statement

Manpreet Kaur: Conceptualization, Methodology, Writing – original draft. **Vijay Kumar:** Writing – original draft. **Kavita Sharma:** Writing – original draft. **Sumant Saini:** Software. **Mukta Sharma:** Writing – review & editing. **Christian Paulik:** Writing – review & editing. **Hideaki Yoshitake:** Writing – review & editing. **Gaurav Rattan:** Writing – review & editing. **Anupama Kaushik:** Conceptualization, Supervision, Writing – review & editing, Funding acquisition.

Declaration of Competing Interest

The authors declare that they have no known competing financial interests or personal relationships that could have appeared to influence the work reported in this paper.

Data availability

Data will be made available on request.

Acknowledgements

The authors acknowledge the financial assistance provided to corresponding author by Council for Scientific & Industrial Research (CSIR) grant no. 22(0798)/19/ EMR-II, Department of Science and Technology (DST), New Delhi (India) for grant numbers SEED/TIASN/008/2018/G and DST/INT/BMWF/Austria/P-03/2020 to carry out this work successfully. The authors are also appreciative the characterization facilities provided by Sophisticated Analytical Instrumentation Facility (SAIF), Panjab University, Chandigarh.

Appendix A. Supplementary data

Supplementary data to this article can be found online at https://doi.org/10.1016/j.seppur.2023.124275.

References

[1] S.-H. Yoo, S.-C. Lee, M. Ko, S. Yoon, J. Lee, J.-A. Park, S.-B. Kim, Adsorption of Hg (II) on polyethyleneimine-functionalized carboxymethylcellulose beads: Characterization, toxicity tests, and adsorption experiments, Int. J. Biol. Macromol. (2023), 124516 Doi:10.1016/j.ijbiomac.2023.124516.

[2] L.T. Budnik, L. Casteleyn, Mercury pollution in modern times and its socio-medical consequences, Sci. Total Environ. 654 (2019) 720–734, https://doi.org/10.1016/j.scitotenv.2018.10.408.

[3] M. Li, S. Zhang, S. Cui, K. Qin, Y. Zhang, P. Li, Q. Cao, H. Xiao, Q. Zeng, Pre-grafting effect on improving adsorption efficiency of cellulose based biosorbent for Hg (II) removal from aqueous solution, Sep. Purif. Technol. 277 (2021), 119493, https://doi.org/10.1016/j.seppur.2021.119493.

[4] C. Wang, Z. Wang, X. Zhang, Y. Gao, H. Zhang, X. Liu, Y. Zhang, Sources and risk assessment of atmospheric Hg during the 2022 Beijing Olympic Winter Games, Atmos. Environ. 302 (2023), 119718, https://doi.org/10.1016/j.atmosenv.2023.119718.

[5] K. Wang, K. Chen, L. Xiang, M. Zeng, Y. Liu, Y. Liu, Relationship between Hg (II) adsorption property and functional group of different thioamide chelating resins, Sep. Purif. Technol. 292 (2022), 121044, https://doi.org/10.1016/j.seppur.2022.121044.

[6] P. Li, X. Feng, G. Qiu, L. Shang, Z. Li, Mercury pollution in Asia: a review of the contaminated sites, J. Hazard. Mater. 168 (2009) 591–601, https://doi.org/10.1016/j.jhazmat.2009.03.031.

[7] Y. Wang, H. Yang, M. Pschenitza, R. Niessner, Y. Li, D. Knopp, A. Deng, Highly sensitive and specific determination of mercury (II) ion in water, food and cosmetic samples with an ELISA based on a novel monoclonal antibody, Anal. Bioanal. Chem. 403 (2012) 2519–2528, https://doi.org/10.1007/s00216-012-6052-1.

[8] M. Li, S. Zhang, P. Zhang, K. Qin, Q. Chen, Q. Cao, Y. Zhang, J. Zhang, C. Yuan, H. Xiao, Dansyl-labelled cellulose as dual-functional adsorbents for elimination and

detection of mercury in aqueous solution via aggregation-induced emission, J. Environ. Manage. 338 (2023), 117773, https://doi.org/10.1016/j.jenvman.2023.117773.
[9] M. Ghaedi, S. Hajjati, Z. Mahmudi, I. Tyagi, S. Agarwal, A. Maity, V. Gupta, Modeling of competitive ultrasonic assisted removal of the dyes–Methylene blue and Safranin-O using Fe3O4 nanoparticles, Chem. Eng. J. 268 (2015) 28–37, https://doi.org/10.1016/j.cej.2014.12.090.
[10] M.M. Matlock, B.S. Howerton, D.A. Atwood, Irreversible precipitation of mercury and lead, J. Hazard. Mater. 84 (2001) 73–82, https://doi.org/10.1016/S0304-3894(01)00190-X.
[11] K. Chakrabarty, P. Saha, A.K. Ghoshal, Simultaneous separation of mercury and lignosulfonate from aqueous solution using supported liquid membrane, J. Membr. Sci. 346 (2010) 37–44, https://doi.org/10.1016/j.memsci.2009.09.010.
[12] S. Chiarle, M. Ratto, M. Rovatti, Mercury removal from water by ion exchange resins adsorption, Water Res. 34 (2000) 2971–2978, https://doi.org/10.1016/S0043-1354(00)00044-0.
[13] B. Zeng, J. Li, C. Xiong, G. Lin, W. Wang, Z. Wu, High-performance Zn-based coordination polymers selectively adsorb mercury ions from aqueous solutions, J. Clean. Prod. (2022), 130551 Doi:10.1016/j.jclepro.2022.130551.
[14] N. Rong, C. Chen, K. Ouyang, K. Zhang, X. Wang, Z. Xu, Adsorption characteristics of directional cellulose nanofiber/chitosan/montmorillonite aerogel as adsorbent for wastewater treatment, Sep. Purif. Technol. 274 (2021), 119120, https://doi.org/10.1016/j.seppur.2021.119120.
[15] N.A. Qasem, R.H. Mohammed, D.U. Lawal, Removal of heavy metal ions from wastewater: A comprehensive and critical review, npj Clean Water 4 (2021) 1–15, https://doi.org/10.1038/s41545-021-00127-0.
[16] N. Shooto, P. Thabede, Binary adsorption of chromium and cadmium metal ions by hemp (Cannabis sativa) based adsorbents, Environ. Nanotechnol. Monit. Manage. 18 (2022), 100683, https://doi.org/10.1016/j.enmm.2022.100683.
[17] M. Monier, I.M. Kenawy, M.A. Hashem, Synthesis and characterization of selective thiourea modified Hg(II) ion-imprinted cellulosic cotton fibers, Carbohydr. Polym. 106 (2014) 49–59, https://doi.org/10.1016/j.carbpol.2014.01.074.
[18] Y. Takagai, A. Shibata, S. Kiyokawa, T. Takase, Synthesis and evaluation of different thio-modified cellulose resins for the removal of mercury (II) ion from highly acidic aqueous solutions, J. Colloid Interface Sci. 353 (2011) 593–597, https://doi.org/10.1016/j.jcis.2010.09.070.
[19] T. Velempini, K. Pillay, X.Y. Mbianda, O.A. Arotiba, Carboxymethyl cellulose thiol-imprinted polymers: Synthesis, characterization and selective Hg (II) adsorption, J. Environ. Sci. 79 (2019) 280–296, https://doi.org/10.1016/j.jes.2018.11.022.
[20] B. Ram, G.S. Chauhan, New spherical nanocellulose and thiol-based adsorbent for rapid and selective removal of mercuric ions, Chem. Eng. J. 331 (2018) 587–596, https://doi.org/10.1016/j.cej.2017.08.128.
[21] Z. Liu, F. Zhen, Q. Zhang, X. Qian, W. Li, Y. Sun, L. Zhang, B. Qu, Nanoporous biochar with high specific surface area based on rice straw digestion residue for efficient adsorption of mercury ion from water, Bioresour. Technol. 359 (2022), 127471, https://doi.org/10.1016/j.biortech.2022.127471.
[22] M. Naushad, T. Ahamad, Z.A. AlOthman, A.a.H. Al-Muhtaseb, Green and eco-friendly nanocomposite for the removal of toxic Hg(II) metal ion from aqueous environment: Adsorption kinetics & isotherm modelling, Journal of Molecular Liquids, 279 (2019) 1-8 Doi:10.1016/j.molliq.2019.01.090.
[23] Y. Sun, Y. Wu, Y. Fu, C. Yang, J. Jiang, G. Yan, J. Hu, Rapid and high selective removal of Hg(II) ions using tannic acid cross-linking cellulose/polyethyleneimine functionalized magnetic composite, Int. J. Biol. Macromol. 182 (2021) 1120–1129, https://doi.org/10.1016/j.ijbiomac.2021.04.091.
[24] H. Ahmad, R. Ahmad Khan, B. Heun Koo, A. Alsalme, Cellulose Nanofibers@ZrO2 membrane for the separation of Hg(II) from aqueous media, J. Phys. Chem. Solid 168 (2022), 110812 Doi:10.1016/j.jpcs.2022.110812.
[25] M. Kaur, P. Tewatia, G. Rattan, S. Singhal, A. Kaushik, Diamidoximated cellulosic bioadsorbents from hemp stalks for elimination of uranium (VI) and textile waste in aqueous systems, J. Hazard. Mater. 417 (2021), 126060, https://doi.org/10.1016/j.jhazmat.2021.126060.
[26] H. Peng, H. Wang, J. Wu, G. Meng, Y. Wang, Y. Shi, Z. Liu, X. Guo, Preparation of superhydrophobic magnetic cellulose sponge for removing oil from water, Ind. Eng. Chem. Res. 55 (2016) 832–838, https://doi.org/10.1021/acs.iecr.5b03862.
[27] M.A. Hussain, T. Liebert, T. Heinze, Acylation of Cellulose with N, N′-Carbonyldiimidazole-Activated Acids in the Novel Solvent Dimethyl Sulfoxide/Tetrabutylammonium Fluoride, Macromol. Rapid Commun. 25 (2004) 916–920, https://doi.org/10.1002/marc.200300308.
[28] M.C. Nagel, T. Heinze, Esterification of cellulose with acyl-1H-benzotriazole, Polym. Bull. 65 (2010) 873–881, https://doi.org/10.1007/s00289-010-0250-9.
[29] M.R. Shamsuddin, S.N. Fauzee, F.H. Anuar, I. Abdullah, R. Othaman, Modification of cellulose by polymethyl methacrylate grafting for membrane applications, Jurnal Teknologi 65 (2013).
[30] K. Cheng, B. Goydish, 4, 4′-Bis (dimethylamino) thiobenzophenone as a sensitive reagent for mercury and palladium, Microchem. J. 10 (1966) 158–170, https://doi.org/10.1016/0026-265X(66)90203-7.
[31] P.M. Pakdel, S.J. Peighambardoust, N. Arsalani, H. Aghdasinia, Safranin-O cationic dye removal from wastewater using carboxymethyl cellulose-grafted-poly (acrylic acid-co-itaconic acid) nanocomposite hydrogel, Environ. Res. 212 (2022), 113201, https://doi.org/10.1016/j.envres.2022.113201.
[32] J. Chen, G. Li, Y. Huang, H. Zhang, H. Zhao, T. An, Optimization synthesis of carbon nanotubes-anatase TiO2 composite photocatalyst by response surface methodology for photocatalytic degradation of gaseous styrene, Appl Catal B 123 (2012) 69–77, https://doi.org/10.1016/j.apcatb.2012.04.020.
[33] M.T. Al-Shemy, A. Al-Sayed, S. Dacrory, Fabrication of sodium alginate/graphene oxide/nanocrystalline cellulose scaffold for methylene blue adsorption: Kinetics and thermodynamics study, Sep. Purif. Technol. 290 (2022), 120825.
[34] S.K. Lagergren, About the theory of so-called adsorption of soluble substances, Sven. Vetenskapsakad. Handingarl 24 (1898) 1–39.
[35] H. Qiu, L. Lv, B.-C. Pan, Q.-J. Zhang, W.-M. Zhang, Q.-X. Zhang, Critical review in adsorption kinetic models, Journal of Zhejiang University-Science A 10 (2009) 716–724, https://doi.org/10.1631/jzus.A0820524.
[36] M.A. Al-Ghouti, D.A. Da'ana, Guidelines for the use and interpretation of adsorption isotherm models: A review, J. Hazard. Mater. 393 (2020), 122383, https://doi.org/10.1016/j.jhazmat.2020.122383.
[37] A. Dada, A. Olalekan, A. Olatunya, O. Dada, Langmuir, Freundlich, Temkin and Dubinin–Radushkevich isotherms studies of equilibrium sorption of Zn2+ unto phosphoric acid modified rice husk, IOSR Journal of applied chemistry, 3 (2012) 38-45https://doi.org/10.9790/5736-0313845.
[38] W. Li, B. Ju, S. Zhang, A green l-cysteine modified cellulose nanocrystals biosorbent for adsorption of mercury ions from aqueous solutions, RSC Adv. 9 (2019) 6986–6994, https://doi.org/10.1039/C9RA00048H.
[39] D. Sachdev, P.K. Jha, R. Rani, G. Verma, N. Kaur, O. Sahu, Structural and optical investigation of highly fluorescent tartaric acid derived from the tamarind pulp, Mater. Chem. Phys. (2023), 127294, https://doi.org/10.1016/j.matchemphys.2023.127294.
[40] R. Ceaser, A.F. Chimphango, Comparative analysis of physical and functional properties of cellulose nanofibers isolated from alkaline pre-treated wheat straw in optimized hydrochloric acid and enzymatic processes, Int. J. Biol. Macromol. 171 (2021) 331–342, https://doi.org/10.1016/j.ijbiomac.2021.01.018.
[41] M. Bansal, G.S. Chauhan, A. Kaushik, A. Sharma, Extraction and functionalization of bagasse cellulose nanofibres to Schiff-base based antimicrobial membranes, Int. J. Biol. Macromol. 91 (2016) 887–894, https://doi.org/10.1016/j.ijbiomac.2016.06.045.
[42] J.T. Mhlongo, Y. Nuapia, M.M. Motsa, T.O. Mahlangu, A. Etale, Green chemistry approaches for extraction of cellulose nanofibers (CNFs): A comparison of mineral and organic acids, Mater. Today:. Proc. (2022), https://doi.org/10.1016/j.matpr.2022.02.088.
[43] H.Y. Choi, J.H. Bae, Y. Hasegawa, S. An, I.S. Kim, H. Lee, M. Kim, Thiol-functionalized cellulose nanofiber membranes for the effective adsorption of heavy metal ions in water, Carbohydr. Polym. 234 (2020), 115881, https://doi.org/10.1016/j.carbpol.2020.115881.
[44] G. Lin, C. Wang, X. Li, Y. Xi, W. Wang, L. Zhang, J. Chang, Synthesis of coordination polymer by 2, 2′-dithiodipropionic acid and selective removal of Hg (ii)/Pb (ii) in wastewater, J. Taiwan Inst. Chem. Eng. 113 (2020) 315–324, https://doi.org/10.1016/j.jtice.2020.08.037.
[45] X. Chen, J. Chen, T. You, K. Wang, F. Xu, Effects of polymorphs on dissolution of cellulose in NaOH/urea aqueous solution, Carbohydr. Polym. 125 (2015) 85–91, https://doi.org/10.1016/j.carbpol.2015.02.054.
[46] M. Song, W. Li, X. Zhang, J. Liu, K. Li, H. Zhang, Structural stability of L-cystine under extreme conditions, ACS Earth Space Chem. 5 (2021) 1525–1534, https://doi.org/10.1021/acsearthspacechem.1c00068.
[47] M. Shamsipur, S.M. Pourmortazavi, M. Roushani, I. Kohsari, S.S. Hajimirsadeghi, Novel approach for electrochemical preparation of sulfur nanoparticles, Microchim. Acta 173 (2011) 445–451, https://doi.org/10.1007/s00604-011-0581-8.
[48] S. Ouajai, R. Shanks, Composition, structure and thermal degradation of hemp cellulose after chemical treatments, Polym. Degrad. Stab. 89 (2005) 327–335, https://doi.org/10.1016/j.polymdegradstab.2005.01.016.
[49] O.M. Vanderfleet, M.S. Reid, J. Bras, L. Heux, J. Godoy-Vargas, M.K. Panga, E. D. Cranston, Insight into thermal stability of cellulose nanocrystals from new hydrolysis methods with acid blends, Cellul. 26 (2019) 507–528, https://doi.org/10.1007/s10570-018-2175-7.
[50] Y.G. Yoo, S. Park, S. Bae, J. Park, I. Nam, J. Yi, Transition metal-free graphene framework based on disulfide bridges as a Li host material, Energy Storage Mater. 14 (2018) 238–245, https://doi.org/10.1016/j.ensm.2018.04.007.
[51] D. Zhang, L. Wang, H. Zeng, P. Yan, J. Nie, V.K. Sharma, C. Wang, A three-dimensional macroporous network structured chitosan/cellulose biocomposite sponge for rapid and selective removal of mercury (II) ions from aqueous solution, Chem. Eng. J. 363 (2019) 192–202.
[52] J. Guo, H. Tian, J. He, Integration of CuS nanoparticles and cellulose fibers towards fast, selective and efficient capture and separation of mercury ions, Chem. Eng. J. 408 (2021), 127336, https://doi.org/10.1016/j.cej.2020.127336.
[53] P. Tapangpan, N. Chiangraeng, S.A. Boer, N. Semakul, P. Nimmanpipug, A. Rujiwatra, Mercury removal efficiency of disulfide-and thiol-functionalized lanthanide coordination polymers, Chemosphere 305 (2022), 135330.
[54] L. Fan, A. Zhou, L. Zhong, Z. Zhang, Y. Liu, Selective and effective adsorption of Hg (II) from aqueous solution over wide pH range by thiol functionalized magnetic carbon nanotubes, Chemosphere 226 (2019) 405–412, https://doi.org/10.1016/j.chemosphere.2019.03.154.
[55] Q. Kong, C. Wei, S. Preis, Y. Hu, F. Wang, Facile preparation of nitrogen and sulfur co-doped graphene-based aerogel for simultaneous removal of Cd2+ and organic dyes, Environ. Sci. Pollut. Res. 25 (2018) 21164–21175, https://doi.org/10.1007/s11356-018-2195-8.
[56] F.P. Fato, D.-W. Li, L.-J. Zhao, K. Qiu, Y.-T. Long, Simultaneous Removal of Multiple Heavy Metal Ions from River Water Using Ultrafine Mesoporous Magnetite Nanoparticles, ACS Omega 4 (2019) 7543–7549, https://doi.org/10.1021/acsomega.9b00731.
[57] R.G. Pearson, The HSAB principle—more quantitative aspects, Inorg. Chim. Acta 240 (1995) 93–98.

[58] H. Nakayama, S. Hirami, M. Tsuhako, Selective adsorption of mercury ion by mercaptocarboxylic acid intercalated Mg–Al layered double hydroxide, J. Colloid Interface Sci. 315 (2007) 177–183, https://doi.org/10.1016/j.jcis.2007.06.036.
[59] P. Beslin, P. Metzner, Y. Vallée, J. Vialle, Cis-selectivity of the kinetic deprotonation of dithiopropanoates, Tetrahedron Lett. 24 (1983) 3617–3620, https://doi.org/10.1016/S0040-4039(00)88183-6.
[60] L. Guo, H. Yan, Z. Chen, Q. Liu, Y. Feng, F. Ding, Y. Nie, Amino functionalization of reduced graphene oxide/tungsten disulfide hybrids and their bismaleimide composites with enhanced mechanical properties, Polymers 10 (2018) 1199.
[61] A. Hashem, L.A. Mohamed, A. Fletcher, M. Sanousy, H. Younis, H. Mauof, Carboxylated cellulose for adsorption of Hg (II) ions from contaminated water: isotherms and kinetics, J. Polym. Environ. 29 (2021) 3040–3053, https://doi.org/10.1007/s10924-021-02075-9.
[62] S. Lai, Y. Jin, L. Shi, Y. Li, R. Zhou, Tailoring multifunctional gel for sensitive naked-eye and fluorescence dual-mode detection and effective adsorption of cadmium (II) and lead (II) ions in water, Chem. Eng. J. 429 (2022), 132367, https://doi.org/10.1016/j.cej.2021.132367.
[63] C. Jiao, Z. Zhang, J. Tao, D. Zhang, Y. Chen, H. Lin, Synthesis of a poly (amidoxime-hydroxamic acid) cellulose derivative and its application in heavy metal ion removal, RSC Adv. 7 (2017) 27787–27795, https://doi.org/10.1039/C7RA03365F.
[64] H. Liu, R. Sun, S. Feng, D. Wang, H. Liu, Rapid synthesis of a silsesquioxane-based disulfide-linked polymer for selective removal of cationic dyes from aqueous solutions, Chem. Eng. J. 359 (2019) 436–445, https://doi.org/10.1016/j.cej.2018.11.148.